



BRNO UNIVERSITY OF TECHNOLOGY

VYSOKÉ UČENÍ TECHNICKÉ V BRNĚ

FACULTY OF MECHANICAL ENGINEERING

FAKULTA STROJNÍHO INŽENÝRSTVÍ

INSTITUTE OF PHYSICAL ENGINEERING

ÚSTAV FYZIKÁLNÍHO INŽENÝRSTVÍ

OPTICAL DICHROISM IN VORTEX ELECTRON ENERGY-LOSS SPECTROSCOPY

OPTICKÝ DICHROISMUS VE SPEKTROSKOPII ENERGOVÝCH ZTRÁT VORTEXOVÝCH ELEKTRONŮ

BACHELOR'S THESIS

BAKALÁŘSKÁ PRÁCE

AUTHOR

AUTOR PRÁCE

Martin Ošmera

SUPERVISOR

VEDOUCÍ PRÁCE

Ing. Andrea Konečná, Ph.D.

BRNO 2022

Assignment Bachelor's Thesis

Institut: Institute of Physical Engineering
Student: **Martin Ošmera**
Degree programm: Physical Engineering and Nanotechnology
Branch: no specialisation
Supervisor: **Ing. Andrea Konečná, Ph.D.**
Academic year: 2021/22

As provided for by the Act No. 111/98 Coll. on higher education institutions and the BUT Study and Examination Regulations, the director of the Institute hereby assigns the following topic of Bachelor's Thesis:

Optical dichroism in vortex electron energy–loss spectroscopy

Brief Description:

Transmission electron microscopy is one of the fundamental techniques suitable not only for imaging samples with atomic resolution but it can also be used together with spectroscopic techniques, such as electron energy–loss spectroscopy, which is capable of detecting energy transfer between the electron beam and probed sample. One of the new possibilities is to employ vortex electron beams, which in the interaction with samples exchange energy and also orbital angular momentum that is manifested in dichroism in electron energy–loss spectra. The use of electron vortices is especially suitable for probing chiral or magnetic samples whose response would be otherwise undetectable.

In this thesis, the interaction of vortex electrons with chiral nanostructures (e.g. plasmonic antennas of special shapes) will be explored. Both numerical and analytical descriptions will be used in limiting cases. One of the possible goals will be to find experimental conditions and parameters (e. g. focusing of the beam, magnitude of the orbital angular momentum, initial beam energy) for maximization of the detected dichroic signal.

Bachelor's Thesis goals:

- 1) Review of electron energy–loss spectroscopy (EELS) and vortex electron beams (VEBs). Study the possibilities of theoretical description of inelastic interaction of VEBs with different types of samples.
- 2) Model analytically EELS for VEBs interacting with point chiral objects. Try to find computationally suitable experimental parameters for the maximisation of dichroic EELS signal.
- 3) Get to know existing programmes for the numerical solution of Maxwell's equations (e.g., Comsol Multiphysics, MNPBEM toolbox for Matlab) and try to implement the interaction of VEBs with chiral nanostructures within these programmes.

Recommended bibliography:

GARCÍA DE ABAJO, F. J. Optical excitations in electron microscopy. *Rev. Mod. Phys.*, 82 (2010), 209-275.

ASENJO-GARCÍA A., and GARCÍA DE ABAJO, F. J. Dichroism in the interaction between vortex electron beams, plasmons, and molecules. *Phys. Rev. Lett.*, 113 (2014), 066102.

ZANFROGNINI, M., et al. Orbital angular momentum and energy loss characterization of plasmonic excitations in metallic nanostructures in TEM. *ACS Photonics*, 6 (2019), 620-627.

Deadline for submission Bachelor's Thesis is given by the Schedule of the Academic year 2021/22

In Brno,

L. S.

prof. RNDr. Tomáš Šikola, CSc.
Director of the Institute

doc. Ing. Jaroslav Katolický, Ph.D.
FME dean

Abstract

Vortex electron beams (VEBs) carry orbital angular momentum and when they interact with a chiral specimen, dichroism can be observed. In electron energy loss spectroscopy, left-handed VEBs yield different spectra than right-handed VEBs. This could be utilized in the analysis of chiral molecules or nanostructures. We present a semianalytical fully-retarded model for the interaction of a non-focused VEB with a point-like particle, and a numerical quasistatic model for the interaction of a non-focused VEB with a “macroscopic” chiral nanostructure.

Key Words

Vortex electron beams, Electron energy loss spectroscopy, Orbital angular momentum, Chirality, Dichroism, Nanophotonics.

Abstrakt

Vortexové elektronové svazky (VES) nesou orbitální moment hybnosti a při jejich interakci s chirálními strukturami lze pozorovat dichroismus. Ve spektroskopii energiových ztrát elektronů získáme použitím levotočivých VES jiná spektra, než v případě pravotočivých. Tohoto jevu lze využít například v analýze chirálních molekul nebo nanostruktur. Předkládáme semianalytický plně retardovaný model interakce nefokusovaného VES s bodovou chirální polarizovatelnou částicí a numerický kvazistatický model interakce nefokusovaného VES s chirální „makroskopickou“ nanostrukturou.

Klíčová slova

Vortexové elektronové svazky, Spektroskopie energiových ztrát elektronů, Orbitální moment hybnosti, Chiralita, Dichroismus, Nanofotonika.

OŠMERA, Martin. *Optical dichroism in vortex electron energy-loss spectroscopy*. Brno, 2022. URL: <https://www.vutbr.cz/studenti/zav-prace/detail/139390>. Bachelor's thesis. Brno University of Technology, Faculty of Mechanical Engineering, Institute of Physical Engineering. Supervisor Andrea Konečná.

Hereby I declare that I have created this work autonomously under the scientific supervision of Ing. Andrea Konečná, Ph.D. All sources, references and literature used or excerpted during the elaboration of this work are properly cited and listed in the complete reference.

Martin Ošmera



Acknowledgement

My sincere thanks belong to Andrea who helped me indescribably with the understanding of all the exciting physics used (not only) in this thesis. Our talks were very inspiring and enjoyable and I can not imagine writing my bachelor's thesis under the supervision of anyone else. I would like to thank my little yellow duckling, Jirka, and all my friends from FyzIng for the time spent with them and all the help they have provided me. I would not be able to complete my Bachelor's studies without them. I would also like to thank my family for the food they gave me so i did not die and could grow up. Finally, a deep thank you belongs to my elven princess, who supported me unconditionally when I changed my study programme to Physical Engineering. I thank you, my little fox, for all the love you gave me.

Martin Ošmera

Contents

Introduction	1
1 Electron Energy-Loss Spectroscopy with Vortex Electron Beams	3
1.1 Vortex Electron Beams (VEBs)	4
1.1.1 Theoretical Description of VEB Formation	6
1.1.2 Handedness Convention	9
1.1.3 Practical Methods of VEB Preparation	9
1.2 Inelastic Interaction of a VEB with a Point-like Polarizable Particle	12
1.2.1 Modelled Experimental Setup	12
1.2.2 Energy Loss Probability Spectrum	13
1.3 About Electron Energy Loss Spectroscopy	17
2 Semi-Analytical Model of VEB's Interaction with a Chiral Point Object	19
2.1 Green's Response Tensor	19
2.1.1 Drude Model for Relative Permittivity	23
2.1.2 Polarizability Tensor of a Sphere	23
2.2 Implementation	24
2.3 Results	26
3 Numerical Model	33
3.1 Boundary Element Method	34
3.2 Interaction of Electron Beam with the Specimen	35
3.3 Implementation	36
3.4 Results	40
Summary	47
Appendices	47
A Mathematical Notes	49
A.1 Square Root Approximation	49
A.2 Cylindrical Coordinates	49
A.3 Evaluation of Integral (1.16) Using Jacobi–Anger Expansion	50
List of Abbreviations	51
References	53

Introduction

Today's society is heavily dependent on technology. We use a variety of special materials, electronic devices or drugs to make our lives easier, healthier and more enjoyable. These improvements are possible thanks to science, engineering and medicine. Science studies nature and searches for rules and laws which govern our universe. Engineers, physicians and scientists then apply the principles they find and create novel inventions which often become an everyday need for most of us. To understand nature, we need to observe it. Our sight, smell, hearing and other senses are, unfortunately, very limited in the signals they can receive. We also evolved to understand the world mainly qualitatively, not quantitatively. In general, we cannot perceive things we do not need to (or cannot) interact with actively. The world, however, is made up of little things. To understand it, we have to overcome the limits of our senses. In the case of sight, we started with optical microscopes. As we zoomed in more and more, we eventually found out that the light could not be focused indefinitely. Another disadvantage of an optical microscope is that we can retrieve only information gained from the visible light transmitted through or reflected or diffracted from the specimen. Often, however, we want also information about different properties of the specimen, e.g. material composition.

These problems were overcome by Ernst Ruska who engineered the first electron microscope. Electrons are particles with a non-zero rest mass. Thanks to that, we can get the same spatial resolution with much less energy in imaging with electrons compared to light. It is also incomparably easier to manipulate (focus) charged particles as electrons compared to high-energy electromagnetic radiation such as x-rays.

Another advantage of electron microscopy is our ability to collect different signals from the measurement. One of the methods realized in Scanning Transmission Electron Microscopy (STEM) is Electron Energy Loss Spectroscopy (EELS), which stands at the end of this thesis title. EELS is a spectroscopic method which means that the result of the measurement is a spectrum of probability that the electron loses specific energy in the interaction with the specimen.

Electron beams in microscopes are focused and shaped by electron optics to gain the best possible spatial resolution and the sharpest energy distributions of electrons. In the last decade, we witnessed an emergence of beam shaping both in the amplitude and in the phase of electron beam wavefront. These so-called shaped beams or beams with tailored wave functions open new possibilities in imaging and spectroscopy.

One particular kind of shaped beam is a vortex electron beam (VEB) (which also stands in the title of this thesis). The VEBs have a phase singularity thanks to which they carry an orbital angular momentum (OAM). The symmetry of such a beam is thus smaller compared to a conventional electron beam, and it can interact with the specimen via different mechanisms. Intuitively stated, such an electron acts not only as a moving charge but also as a moving magnetic dipole. Using the VEBs brings a new degree of freedom to specimen

analysis.

VEBs are inherently chiral, meaning there exists a right-handed VEB and its mirror image, a left-handed VEB, which are not identical. Nature (and the man-made world too) is full of chiral structures. When a chiral structure interacts with another chiral structure, a phenomenon called dichroism often appears. ("Dichroism" is also a part of the title of this thesis. The last part not already mentioned is the word "optical" which says that we are interested in energies corresponding to visible light.) By the term dichroism, we refer to the difference between interactions of a structure with left-handed vs. right-handed impulses (in our case provided by VEBs).

Multifariousness of natural objects is chiral. These can be of macroscopic size (e.g. shells of animals or their body parts, such as human hands from whose name in Greek – $\chi\epsilon\iota\rho$ – chirality got its name) or microscopic. Microscopic chiral structures can be found for example on insect scrubs where they are responsible for the beautiful colours we can see. Very frequently, we also encounter chiral molecules, including DNA, amino acids, proteins or saccharides and polysaccharides. Studying such molecules is very important especially in medicine since different enantiomers of drugs (or endogenous substances) can have different or even completely opposite effects. Some drugs can be teratogenous, like Thalidomide, or carcinogenic in one enantiomer form and medicinal in other. In chemistry or material science, chirality is studied too since it can be exploited in the design of metamaterials. VEBs are proposed as a great tool for probing chiral structures including single molecules.

Man-made things are often chiral on purpose. In nanophotonics, fabricating and understanding the functionalities of chiral structures have great potential for the measurement of the concentration or state of chiral molecules. This could be very beneficial in medicine.

This thesis is purely theoretical. We propose two experiments and model them. In both experiments, we assume a non-focused Bessel vortex beam interacting with a specimen.

The first experiment is discussed in Ch. 2 and partially in Ch. 1. In this experiment, a non-focused (in contrast to previous works) VEB with a defined OAM interacts with a point-like particle characterized by a polarizability tensor. This tensor describes how the specimen polarizes electrically and magnetically by electric and magnetic fields. We show that the dichroism emerges when non-zero "crossed" polarizabilities (meaning that magnetic dipole is induced by an electric field and vice versa) are present. We study the dependence of dichroic spectra on several parameters including the initial and final (i.e. the change of) topological charge and position of the polarizable particle. The model is semi-analytical and we used Python to implement the numerical part of the computation. This model should reflect an experiment in which chiral molecules are studied directly by an electron beam.

Another experiment, in which a "big" (few tens of nm in size) chiral nanophotonic structure is studied by non-focused VEB, is proposed in Ch. 3. We model the interaction of a VEB with two silver nanorods by numerically extracting plasmonic eigenmodes from MNPBEM toolbox for Matlab and processing them in Python scrips developed within this thesis. This experiment is modelled in quasistatic approximation but since the studied structure is very small, the results should apply to a possible experiment.

In both cases, we propose an initial phase plate by which one specific VEB with a well-defined OAM is prepared. After the interaction with a specimen, we then propose employment of an OAM filter. This filter chooses only one particular vortex state from the superposition of all possible states in which the electron is after the interaction.

Chapter 1

Electron Energy-Loss Spectroscopy with Vortex Electron Beams

Over the last century, the need of mankind to look at small things grew rapidly. One of the approaches used to gain better spatial resolution is to utilize electrons instead of photons. The first step in electron microscopy is the generation of free electrons. This is done by pulling the electrons from a cathode by an electric field. The cathode can be heated to lower the difference between the thermal energy of the electrons in the specimen and the work function of the cathode. However, in state-of-the-art designs of electron microscopes, cold (room temperature) cathode and the so-called field emission process is used, mainly because the resulting electron beam has a narrower energy distribution.

Electrons pulled from the cathode are then collimated and shaped into a well-controlled beam. Electron optics consisting of electrostatic and magnetostatic lenses is used to focus and further manipulate the beam e. g. for scanning. The beam profile can be further modified for different uses. Nowadays, beam currents can be so low that less than one electron is present in the microscope column at one moment. The beam amplitude profile can be then understood as the square modulus of the electron's wave function. As we will demonstrate in Secs. 1.1.1 and 1.1.3 electron beams can be tailored not only in amplitude but in the phase domain, too.

There are generally two types of electron microscope designs, scanning and transmission. In a Scanning Electron Microscope (SEM) the electron beam is scanned over the specimen and different types of emitted particles (e.g. secondary electrons, Auger electrons, backscattered electrons, cathodoluminescence, x-ray etc.) are detected, revealing different pieces of information about the point on the specimen in which the beam is currently directed. The image is then constructed by attributing the measured signal to each point of the rastered mesh. The specimen can be thick (it has to fit into the microscope chamber) but must be conductive. Non-conductive specimens are thus covered by a thin metallic layer.

The second class of electron microscopes are Transmission Electron Microscopes (TEMs) which work similarly to traditional optical microscopes in which the light transmits through the specimen. Transmitted electrons construct an image on a fluorescent screen captured by a camera or directly on a CCD chip. Should electrons pass through the specimen, we typically need much higher accelerating voltage and very thin specimens ($\lesssim 100$ nm, this is probably the main disadvantage of TEM). Electrons in a typical TEM have energies around 30 keV (with speed $0.33c$, where c is the speed of light in vacuum) but can reach up to 300 keV ($0.78c$). Such electron beams can be focused to spot with diameter $\lesssim 0.1$ nm [8, 18], which leads to a very good lateral resolution since interatomic distances are typically in

orders of 10^{-1} nm.

There exists an interesting combination of both previous approaches: Scanning Transmission Electron Microscopy (STEM). In STEM, a high energy electron beam is scanned over a thin specimen. Several signals can be measured: transmitted electrons, high-angle diffracted electrons, cathodoluminescence etc. Besides the topographic view, STEM can be operated in a tomographic mode getting us full 3D spatial information about specimens.

We need not only to see the topography of the specimens but also to characterize their material excitations residing in them (in the best scenario together with the spatial layout). For this purpose, STEM offers several spectroscopic methods (e.g. cathodoluminescence (CL) or energy dispersive x-ray (EDX) spectroscopy). Another widely used technique is Electron Energy-Loss Spectroscopy (EELS) which is preferentially used in Scanning Transmission Electron Microscopy (STEM). This method enables us to characterize and understand the specimen excitations via electron energy loss spectral function (spectrum) (EELSF) which will be discussed later in Sec. 1.3.

1.1 Vortex Electron Beams (VEBs)

Before we present electron vortices (vortex electron beams, VEBs), we should mention their predecessors in light. When circularly polarized, photons carry spin angular momentum $\pm\hbar$ where the sign depends on the direction of spin of the polarization vector. This was shown in 1935 by Beth [3]. Linearly polarized photons can carry angular momentum in the direction of propagation, too. It is called orbital angular momentum (OAM) and is quantized by topological charge l , so that the total OAM magnitude is $l\hbar$. The wavefront of a photon carrying OAM can be written, for instance, as

$$\psi_{\text{LG}}(r, \phi) \propto e^{i l \phi} L(r), \quad (1.1)$$

where $L(r)$ is the Laguerre function dependent, and where the functions depend on polar coordinates r and ϕ [25].

This led physicists to think about an analogue in electron beams. It is known that electrons have spin angular momentum $\pm\hbar/2$. OAM is trivially carried by bound electrons in atoms or molecules. For free electrons, such as those in electron microscopes, the concept of OAM was demonstrated in 2010. First to produce VEBs were Uchida and Tonomura [22] and Verbeeck et al [25]. About the methods of preparation, we further write in Sec. 1.1.3.

Electrons carrying OAM differ from photons in several aspects. They have charge, mass and always carry the spin momentum. They thus react to the electromagnetic field and they can be used to probe circular magnetic dichroism [25]. There is also (as we will explain more deeply later) a possibility to use VEBs to study dichroism in chiral materials and nanostructures. Verbeeck [27] showed that VEBs can be used similarly as optical tweezers to manipulate and rotate nanostructures in space.

In the center of the vortex, there is a phase singularity. This singularity makes the vortex beam chiral, which means that the vortex is not the same as its mirror image, i.e. $\psi_{+l} \neq \psi_{-l}$. In other words, the rotational symmetry around the propagation (optical) axis is broken for VEBs and a new degree of freedom opens in contrast to standard beams.

Chirality can be observed in nature as well. This has enormous importance in biology and chemistry. There exists a lot of molecules such as DNA (deoxyribonucleic acid), proteins, other polymers or simple molecules with four different groups attached to one carbon atom which are chiral. A lot of chiral molecules exist naturally only in one enantiomer, or the

enantiomers have completely different behaviours. If a chiral structure A (e.g. the VEB) interacts with two enantiomorphs of a chiral structure B and \bar{B} , the symmetry is broken and we can expect different responses from the AB vs. $A\bar{B}$ interaction. This phenomenon can be called dichroism and is studied in this thesis. Concretely stated, when probing a chiral structure by VEBs, thanks to the degree asymmetry in the angular coordinate of the beam, we can acquire additional information compared to probing with standard beams.

Electron vortices probably appear commonly in everyday TEM measurements (e.g. in materials with varying thickness) and Uchida suggests they could be used in contrast enhancement [22].

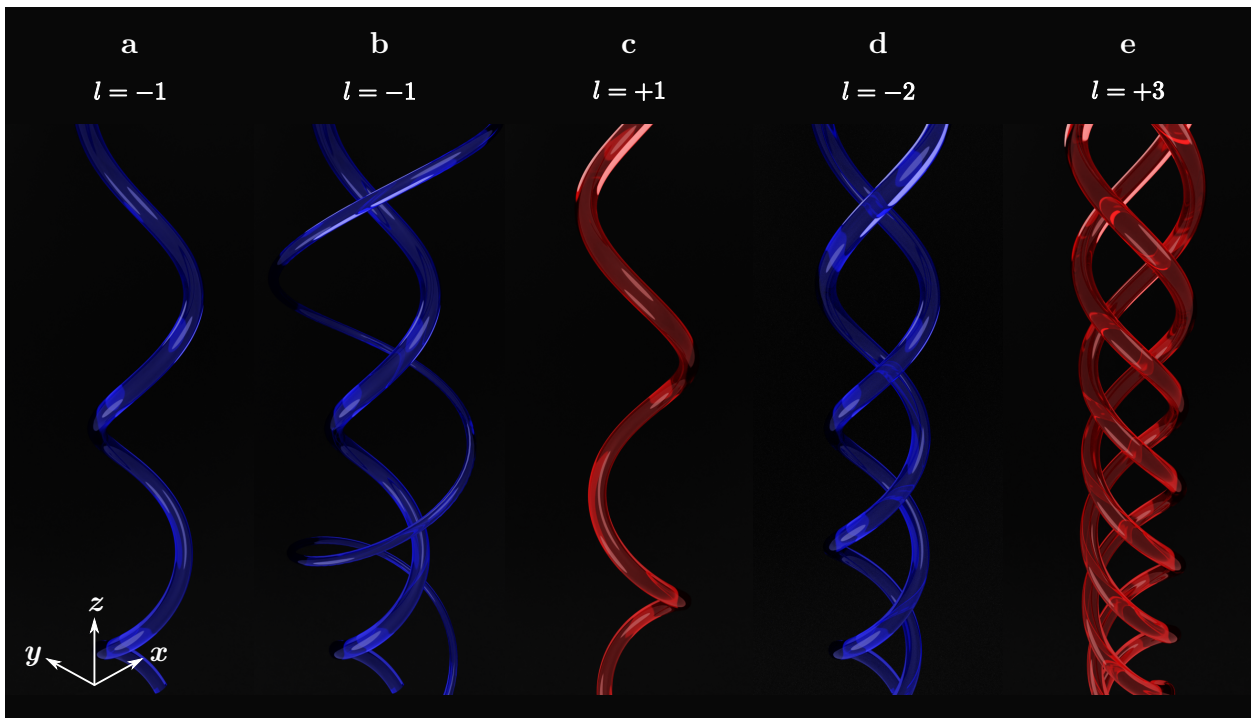


Figure 1.1: Visualizations of VEBs. In this figure we present visualizations of a few VEBs with different topological charges l . These figures can be understood as isosurfaces of the wave functions of depicted VEBs. Note that the left-handed VEBs in blue ($l < 0$) take in space the form of a right-handed helix. In (b) we have pictured also the secondary maximum of the beam. In (d) and (e) one can see that if $|l| > 1$ multiple helices appear.

1.1.1 Theoretical Description of VEB Formation

In this section, we will show a relatively simple derivation of a formula for a wave function corresponding to a VEB used later within this work. We start with the stationary Schrödinger's equation

$$\hat{\mathbf{H}}\psi = E\psi, \quad (1.2)$$

where E is a constant (with the meaning of energy, which does not change through the propagation of the wave, that is why we can use the simpler stationary Eq.) and the Hamiltonian for a free electron of mass m can be written as

$$\hat{\mathbf{H}} = -\frac{\hbar^2}{2m}\nabla^2, \quad (1.3)$$

with \hbar denoting the reduced Planck's constant. It can be shown, by simple substitution into the Schrödinger's Eq. (1.2), that a plane wave propagating along the z axis described as

$$\psi(x, y, z) = \psi(z) = \psi_0 \exp(iq_z z), \quad (1.4)$$

where ψ_0 is a complex amplitude of the wave and q_z its wave vector, is a solution of the equation if and only if

$$E = \frac{\hbar^2 q_z^2}{2m}. \quad (1.5)$$

However, such wave function can not be normalized through the whole space. This should be no problem if we assume that the electron is captured in a finite volume (e.g. the electron microscope), which however has dimensions much larger than the electron wave function's wavelength. Near the center of the potential pit, such wave function will be very similar to the wave function of the free electron. Thus we can normalize the wave function only through the volume of the pit. Similar reasoning can be used in the center of a wavepacket [4].

We now examine the plane wave function impinging on a semi-permeable phase plate. We will consider this plate to be infinitesimally thin, allowing us to describe it by a simple complex function of transmission $T(x', y')$ defined for the x', y' plane perpendicular to z axis at the coordinate z' , in which we have positioned the phase plate as schematically shown in Fig. 1.2. From the law of conservation of energy, such function must fulfil the condition $|T(x', y')| \leq 1$. Concrete real-world realisations of such plates will be discussed in Sec. 1.1.3.

Just after the wave passes through the plate, the wave function changes to $\psi_t = T\psi_i$, where ψ_i is the wave function just before the phase plate. By applying the Huygens principle, every point on the wavefront is by itself a source of a spherical wave. In the paraxial approximation, it is sufficient to consider the wave to spread evenly in all directions. This leads us to solving the diffraction integral.

To find the wave propagating beyond the plane z' to a plane $z > z'$, we can integrate all the contributions of spherical waves coming from points of plane z' . The spherical wave with wave number q coming from a point \mathbf{r}' to a point \mathbf{r} with an initial complex amplitude ψ_0 can be written as

$$\psi_{r'}(\mathbf{r}) = \psi_0 \frac{e^{iq|\mathbf{r}-\mathbf{r}'|}}{|\mathbf{r}-\mathbf{r}'|}, \quad (1.6)$$

where the denominator is a consequence of the law of conservation of energy. To find the total wave, we need to integrate over all the source points. In our particular case this will be

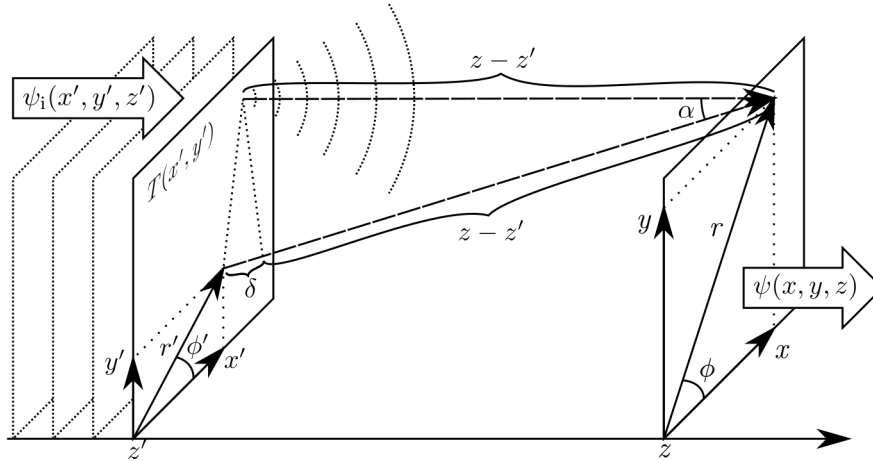


Figure 1.2: Scheme for the construction of the diffraction integral.

the phase plate and using notation depicted in Fig. 1.2, we can find the wave in any point of the z plane as

$$\psi(x, y, z) = -\frac{i q_z}{2\pi} \iint dx' dy' \psi_i(x', y', z') T(x', y') \frac{e^{i q_z(z-z'+\delta)}}{z-z'+\delta}, \quad (1.7)$$

where we have assumed that electron is moving mainly along z axis so that $q_x, q_y \ll q_z \approx q$. The prefactor $-i q_z/2\pi$ corrects the amplitude and phase of the secondary waves, as shown in [13].

Being in the paraxial space, we may use the square root approximation rule (see A.1) and from the geometry of the problem, we can find the path deviation δ (which is responsible for the interference at z plane) as

$$\delta = |\mathbf{r} - \mathbf{r}'| - (z - z') = (z - z') \left[\sqrt{1 + \frac{(x - x')^2 + (y - y')^2}{(z - z')^2}} - 1 \right] \approx \frac{(x - x')^2 + (y - y')^2}{2(z - z')}. \quad (1.8)$$

Thanks to the paraxial approximation, we can assume that for the denominator of the integrand in Eq. (1.7) $z - z' + \delta \approx z - z'$. With these simplifications, we can pull some terms in front of the integral and get

$$\psi(x, y, z) = -\frac{i q_z}{2\pi} \frac{e^{i q_z(z-z')}}{z - z'} \iint dx' dy' \psi_i(x', y', z') T(x', y') \exp \left[i q_z \frac{(x - x')^2 + (y - y')^2}{2(z - z')} \right]. \quad (1.9)$$

From now on, it will be convenient to work in cylindrical coordinates. Using the transformation rules (see A.2) we get the integral in Eq. (1.7) transformed as

$$\begin{aligned} \psi(r, \phi, z) = & -\frac{i q_z}{2\pi} \frac{\exp \left[i q_z \left(z - z' + \frac{r^2}{2(z - z')} \right) \right]}{z - z'} \\ & \times \iint r' dr' d\phi' \psi_i(r', \phi', z') T(r', \phi') \exp \left[\frac{i q_z}{2(z - z')} (r'^2 - 2 r r' \cos(\phi - \phi')) \right]. \end{aligned} \quad (1.10)$$

If we now assume that the wave incident on phase plate is a simple plane wave $\psi_i(r', \phi', z') = \psi'_0 \exp(i q_z z')$ in the z' plane, we can write

$$\begin{aligned} \psi(r, \phi, z) = & -\frac{i q_z \psi_0 \exp(i q_z z)}{2\pi (z - z')} \exp\left(\frac{i q_z r^2}{2(z - z')}\right) \\ & \times \iint r' dr' d\phi' T(r', \phi') \exp\left[\frac{i q_z}{2(z - z')} (r'^2 - 2 r r' \cos(\phi - \phi'))\right]. \end{aligned} \quad (1.11)$$

The equation above is still rather universal. All possible transmission functions can be used to get multifarious results of outgoing waves. Also, it is possible for multiple different T 's to result in similar waves. We shall now have a look at a particular example, where the transmission function takes the form

$$T(r', \phi') = e^{i l \phi'} \quad \text{for } l \in \mathbb{Z}. \quad (1.12)$$

This transmission function characterizes a non-absorbing ($|T| = 1$ in every point) phase plate with a singularity in the middle. It might be surprising that such a function is practically well-achievable, as we'll show later. Finally, our resulting wave function will be

$$\begin{aligned} \psi_l(r, \phi, z) = & \frac{-i q_z \psi_0 \exp(i q_z z)}{2\pi (z - z')} \exp\left(\frac{i q_z r^2}{2(z - z')}\right) \\ & \times \iint r' dr' d\phi' e^{i l \phi'} \exp\left[\frac{i q_z}{2(z - z')} (r'^2 - 2 r r' \cos(\phi - \phi'))\right]. \end{aligned} \quad (1.13)$$

Analytical solution of the integral above can be found in [1].

In practice, however, the beam from the diffraction plate is often focused by electromagnetic lenses to the specimen plane. Transmission through an ideal thin focusing lens is then described by another exponential function

$$F(r') = \exp\left(-i q_z \frac{r'^2}{2f}\right), \quad (1.14)$$

where f is the focal length of the lens. If the lens plane coincides with the phase plate, its transmission function is added in the original diffraction integral:

$$\begin{aligned} \psi_l(r, \phi, z) = & -\frac{i q_z \psi_0 \exp(i q_z z)}{2\pi (z - z')} \exp\left(\frac{i q_z r^2}{2(z - z')}\right) \iint r' dr' d\phi' e^{i l \phi'} \exp\left(-i q_z \frac{r'^2}{2f}\right) \\ & \times \exp\left(i q_z \frac{r'^2}{2(z - z')}\right) \exp\left[i q_z \frac{-r r' \cos(\phi - \phi')}{z - z'}\right]. \end{aligned} \quad (1.15)$$

If $f = z - z'$, the two exponentials in the first line come off leaving us with

$$\psi_l(r, \phi, z) = -\frac{i q_z \psi_0 \exp(i q_z z)}{2\pi (z - z')} \exp\left(\frac{i q_z r^2}{2(z - z')}\right) \iint r' dr' d\phi' e^{i l \phi'} \exp\left[i q_z \frac{-r r' \cos(\phi - \phi')}{z - z'}\right]. \quad (1.16)$$

As shown in Appendix A.3, the integral in ϕ' can be solved analytically and we obtain

$$\psi_l(r, \phi, z) = -i q_z \frac{i^l \psi_0 \exp(i q_z z)}{z - z'} \exp\left(\frac{i q_z r^2}{2(z - z')}\right) e^{i l \phi} \int_0^R r' dr' J_l\left(-q_z \frac{r r'}{z - z'}\right), \quad (1.17)$$

where R is the radius of the used aperture (i. e. the radius of the phase plate). The last integration can be performed in the wave number $q_{r'}$ domain. We use the following expression for initial VEBs assuming that they are coming from an aperture of radius corresponding to maximal perpendicular wave number Q_a :

$$\psi_l(r, \phi, z) = \frac{e^{il\phi}}{Q_a\sqrt{\pi}} \int_0^{Q_a} dq q J_l(qr). \quad (1.18)$$

1.1.2 Handedness Convention

When talking about electron vortices, it is useful to name them to reflect the sign of the topological charge. Unfortunately, two opposing conventions exist in physics. In our work, we will stick to the convention mostly used in engineering and quantum physics. In this convention, the name corresponds to the manner of temporal rotation of the constant phase vector in one particular plane in space from the point of view of the source. When the thumb points in the direction of the beam and the constant phase vector rotates (temporally) as the fingers of the left hand curl, the vortex is left-handed. Such vortex in our notation (see Eqs. (1.18) or (1.20)) has negative topological charge and thus carries negative OAM. Opposite vortices carrying positive topological charge are thus right-handed.

1.1.3 Practical Methods of VEB Preparation

In this section, we will show that previous theoretical assumptions are reasonable to make since phase plates yielding transmission functions similar to those we postulated in Eq. (1.12) are practically well-achievable.

Several methods of VEB preparation have been demonstrated. The first to prepare VEB intentionally were Uchida and Tonomura in 2010 [22]. They used graphite from a pencil in which they found structures with a thickness singularity in the middle. As the electrons impinging at the phase plate at different transverse coordinate, they penetrate the material of varying thickness. The electrons are then delayed proportionally to the thickness and a vortex can be formed. This, however, is not very practical way of vortex preparation since due to the challenging preparation of such phase plate, it is not easily reproducible.

To measure if they really prepared the vortices, Uchida and Tonomura used electron holography. From it a typical "fork" pattern arises, as is shown in Fig. 1.3b. We can reverse this process and let plane wave impinge on a diffraction grating prepared in the shape of the fork (Fig. 1.3c) using focused ion beam (FIB) milling. This way, we can create vortices of opposite topological charges diverted from the main beam as is shown in Fig. 1.3d [25]. These holograms can be computer-computed and prepared for higher topological charges and used also as OAM filters by diverting the chosen vortex in a specific angle.

Spiral zone plates are similar in the production method (FIB) to the fork phase plates. They take shape shown in Fig. 1.3e. [24, 19] Today, even more sophisticated patterns are being used for measuring sorting vortex states. Such phase plate as shown in [16] could be used as the proposed OAM filter in our experiment.

Vorticity can also be imprinted into the beam by applying electromagnetic (EM) field from surface plasmon polaritons generated by elliptically polarized LASER beam illuminating a circular slit in metal. [23]

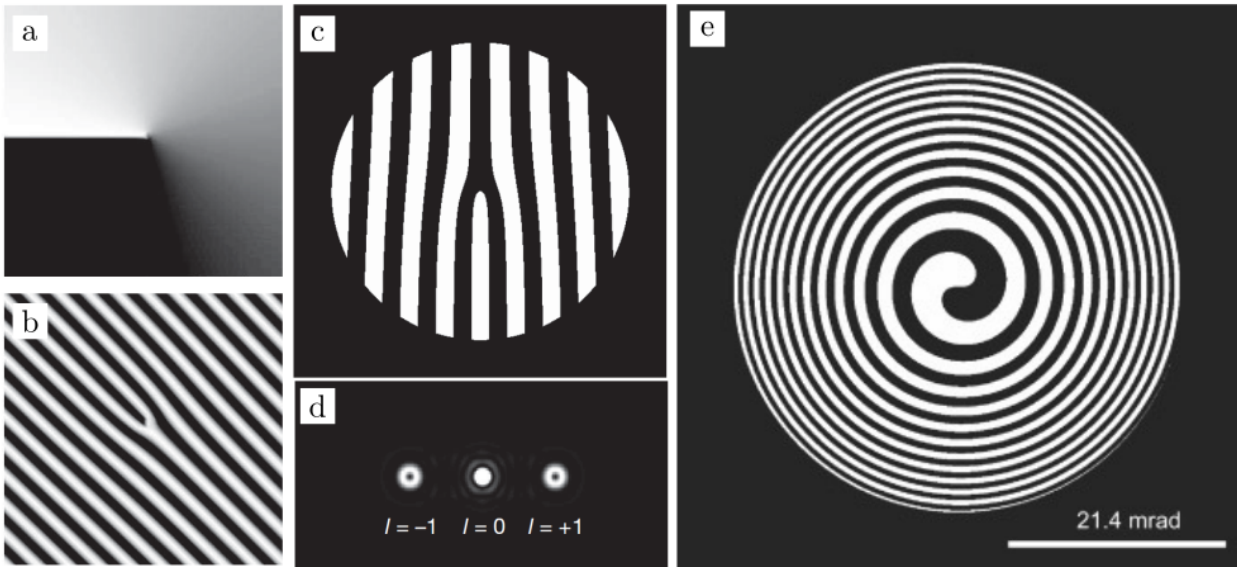


Figure 1.3: Measurement and Preparation of VEBs, Uchida [22] (a,b) and Verbeeck [25, 24] (c,d,e). a) phase profile of an ideal vortex. b) "fork" – hologram formed by interference of $l = 1$ vortex with plane wave. c) "fork" used by Verbeeck to prepare VEBs. d) profile of the beam generated by Verbeeck with diffraction fork in (c). e) spiral zone plate for VEB preparation.

One of the most promising designs of phase plates for preparation of vortex (or other phase-tailored) electrons is a programmable array of microscopic electrodes which can take the form of einzel (unipotential) lenses. Einzel lens consists of three hollow electrodes in a row. The first and the last electrode have the same potential (often they are grounded). The middle electrode has different (and variable) potential. Passing through the lens, the electron effectively slows down (or accelerates) before reverting to the initial speed. This process retards it in phase. Depending on the potential profile forced on the electrodes arranged in an array, phase of the electron wave is delayed differently in different parts of the beam and vortex can be formed from plane wave. [26] In Figs. 1.4 and 1.5 we modelled several VEBs prepared by einzel-lens-PPPs of different designs in a "square-chip" and "cylinders-around-circle" configurations.

More complicated designs of nano-electrode devices enabling the preparation of VEBs with topological charge as high as 1000 have already been showed [20].

1.1. VORTEX ELECTRON BEAMS (VEBS)

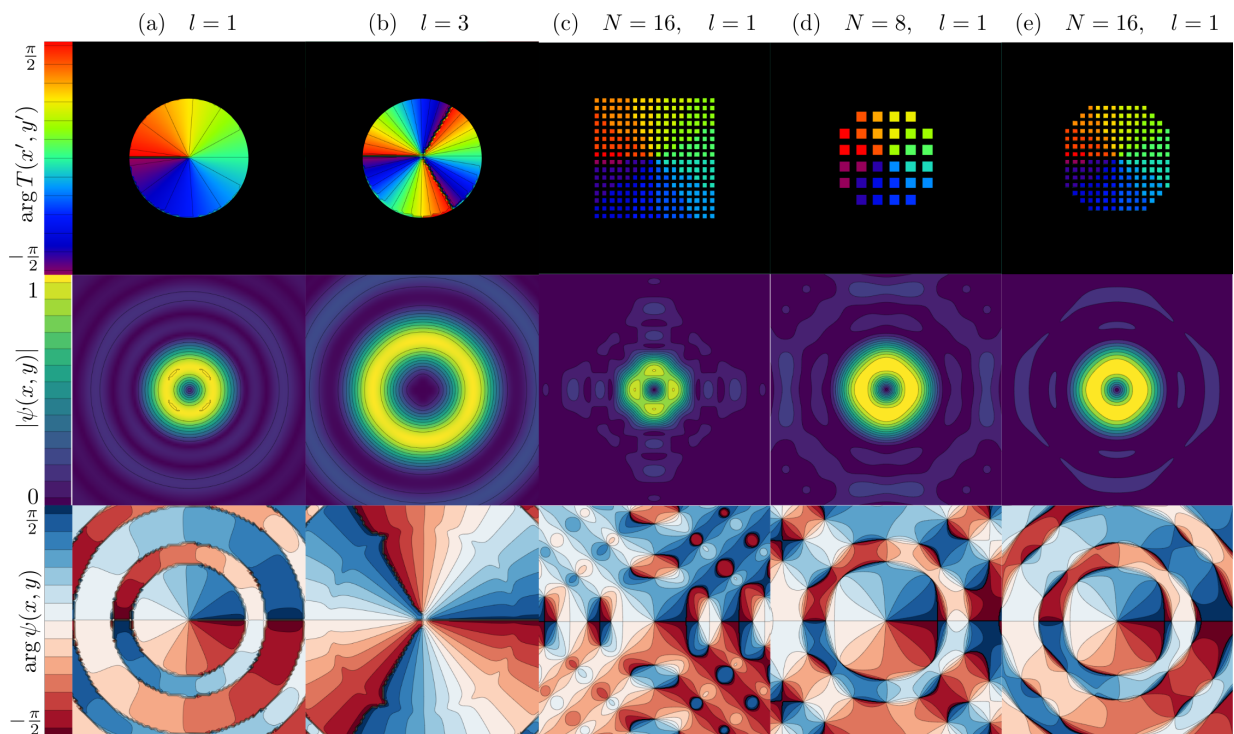


Figure 1.4: Examples of VEBs prepared by ideal phase plates for two different topological charges (a, b) and using a square-matrix of einzel lenses (c, d, e). The imprinted phase is shown in the top row while middle and bottom rows show the resulting wave function amplitude and phase. Note that the wave functions produced in cases (d,e,i) are already quite near the ideal state in (a).

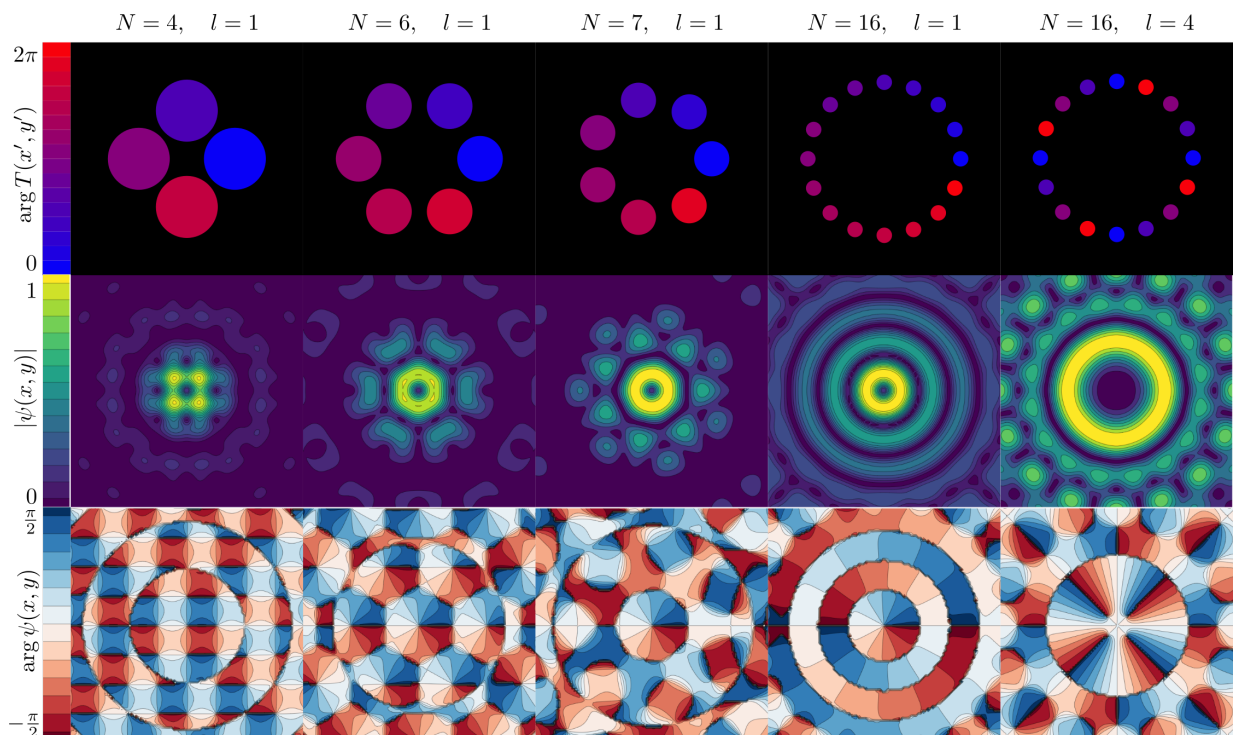


Figure 1.5: Another example of VEBs prepared by round einzel lenses arranged around a circle. Note that for $N = 4$ the square symmetry is manifested significantly. For higher numbers of lenses, however, produced vortices are getting closer to an ideal state.

1.2 Inelastic Interaction of a VEB with a Point-like Polarizable Particle

In this section, we will build on the wave function of the vortex electron beam (VEB) we analyzed in Sec. 1.1 and derive an expression for electron energy loss spectrum (or spectral function EELSF) considering well-defined initial and final vortex states.

1.2.1 Modelled Experimental Setup

The setup of the modelled experiment is captured in Fig. 1.6. VEBs prepared in the beam shaper interact with the specimen and can lose energy and sometimes OAM, which leads to a change of topological charge of the electron. The interaction mechanism is more precisely discussed in Sec. 2.1. After the interaction, the electron is in a superposition of all possible states. From those, one particular vortex state is chosen with an OAM sorter. Such device was already designed in [21]. EELS is then measured for a specific topological charge transition $l_i \rightarrow l_f$.

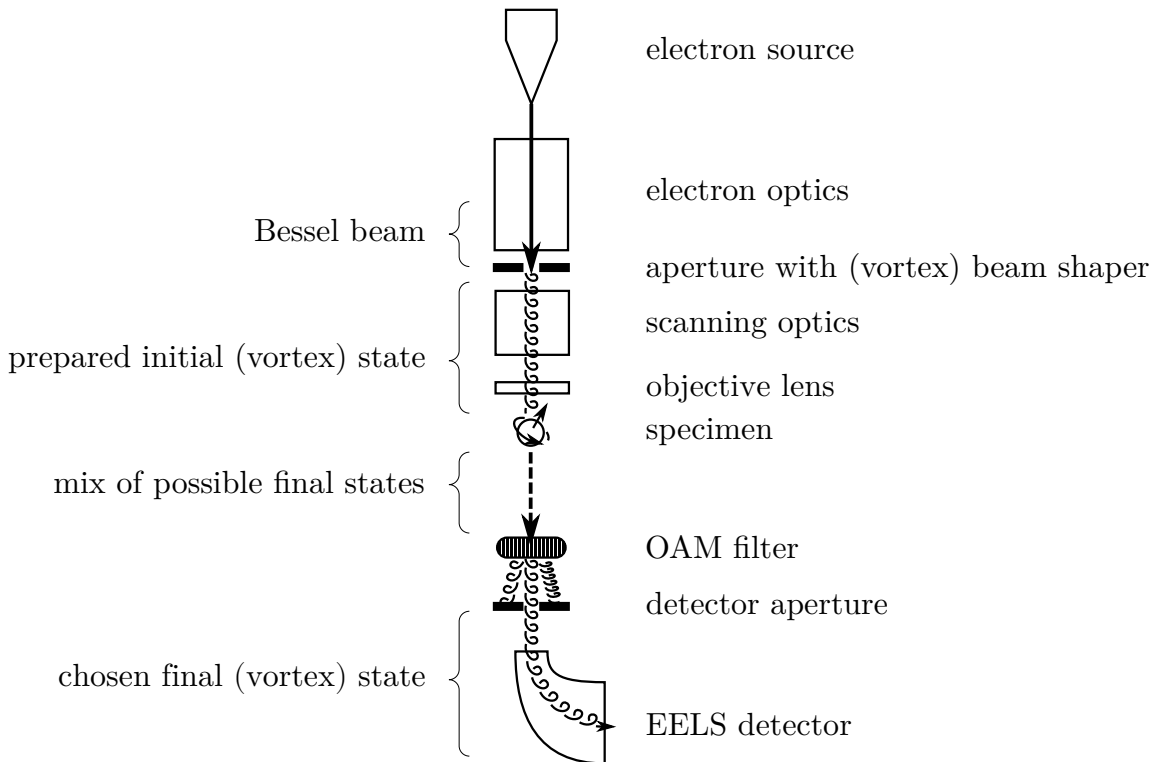


Figure 1.6: A simple schematic of modeled experiment. Electrons from a cathode are accelerated to the desired energy and monochromated (monochromator is not shown in the figure). Traveling through series of optical elements, electrons reach an aperture with a beam shaper (phase plate) and an electron vortex is formed. This electron vortex is projected onto the specimen and interacts with it. With possible use of subsequent optics (not shown), the beam hits an OAM filter which separates a chosen vortex state from the mix emerging from the interaction with specimen. Finally, the electrons are measured by EELS.

1.2.2 Energy Loss Probability Spectrum

Below we present a model based on the first-order perturbation theory. Subsequent paragraphs follow the references [15, 8].

We will work in cylindrical coordinates (r, ϕ, z) , see App. A.2 and consider electrons moving along the z axis. The non-relativistic wave function of VEB with topological charge l can be expressed as a function ψ_l of form

$$\psi_l(r, \phi, z) = \frac{1}{\sqrt{L}} e^{iq_z z} \psi_{l,\perp}(r, \phi). \quad (1.19)$$

Here, we expressed the function as a product of two independent functions. The first being z -dependent phase factor dependent on wave vector's z component $q_z = m_e v / \hbar$ (here expressed as the product of electron's mass m_e and velocity v divided by reduced Planck's constant \hbar) with a normalization prefactor dependent on the normalization length L . The second function can be written as

$$\psi_{l,\perp}(r, \phi) = \frac{1}{\sqrt{A}} e^{il\phi} J_l(q_r r), \quad (1.20)$$

where the normalization prefactor is dependent on the normalization area A and J_l is Bessel function of order l dependent on radial wave vector q_r . The Bessel function is responsible for the radial shape of the vortex. Its phase in the angular direction, i.e. its vorticity, is governed by the exponential term $\exp(il\phi)$.

Such wave function can not be normalized through infinite space, however, similar reasoning as we have discussed below the Eq. (1.5) can be used. Set of these functions for $l \in \mathbb{Z}$ forms a complete basis of possible wave functions with such cylindrical symmetry.¹

It can be shown that Eq. (1.19) is a solution of the Schrödinger equation for a free electron moving along z axis with the static orbital angular momentum (OAM) of magnitude $l\hbar$.

When an electron with the initial energy $\hbar\epsilon_i$ (where ϵ_i is frequency corresponding to the energy) interacts with the specimen, a virtual photon of frequency ω transfers energy $\hbar\omega$ from the electron to the specimen leaving the electron with the final energy $\hbar\epsilon_f$. The interaction mechanism is further discussed in Sec. 2.1 The transition rate from an initial state ψ_i characterized by well-defined initial energy to the final state ψ_f can be expressed using the first order perturbation theory, as [9]

$$\frac{d\Gamma_{i \rightarrow f}}{dt} = \frac{2\hbar e^2}{\omega^2 m^2} \int d^3\mathbf{r} d^3\mathbf{r}' \psi_f(\mathbf{r}) \psi_f^*(\mathbf{r}') \nabla [\psi_i^*(\mathbf{r})] \cdot \text{Im} [\hat{\mathbf{G}}(\mathbf{r}, \mathbf{r}', \omega)] \cdot \nabla [\psi_i(\mathbf{r}')] \delta(\epsilon_f - \epsilon_i + \omega), \quad (1.21)$$

where $\hat{\mathbf{G}}$ is the Green's electromagnetic response tensor of the specimen. We are able to use this equation only if it is possible to construct $\hat{\mathbf{G}}$. For a point-like dipolar particle (for which homogeneous field in its vicinity is considered) the response tensor is discussed in Sec. 2.1.

Consider now an initial state in the form $\psi_i = \exp(iq_{z,i}z)\psi_{\perp,i}(\mathbf{r}_\perp)/\sqrt{L}$ and final state $\psi_f = \exp(iq_{z,f}z)\psi_{\perp,f}(\mathbf{r}_\perp)/\sqrt{L}$. By \mathbf{r}_\perp we denote the z -perpendicular component of position vector. We have also used notation in which gradient is split in derivatives of the perpendicular and longitudinal spatial coordinates $\nabla = [\nabla_\perp; \partial_z]$, where $\nabla_\perp = [\partial_x; \partial_y]$. After substitution of the

¹As we have mentioned earlier, it is possible to use Laguerre functions. In our calculations, however, Bessel functions are sufficient enough and easy to work with.

preceding terms into (1.21), we get

$$\begin{aligned}
\frac{d\Gamma_{i \rightarrow f}}{dt} &= \frac{2\hbar e^2}{L^2 \omega^2 m^2} \int d^3\mathbf{r} d^3\mathbf{r}' e^{i q_{z,f} z} \psi_{f,\perp}(\mathbf{r}_\perp) e^{-i q_{z,f} z'} \psi_{f,\perp}^*(\mathbf{r}'_\perp) \\
&\quad \times e^{-i q_{z,i} z} \left[\nabla_\perp \left\{ \psi_{i,\perp}^*(\mathbf{r}_\perp) \right\}; -i q_{z,i} \psi_{i,\perp}^*(\mathbf{r}_\perp) \right] \cdot \text{Im} \left[\hat{\mathbf{G}}(\mathbf{r}, \mathbf{r}', \omega) \right] \cdot \\
&\quad \times e^{i q_{z,i} z'} \left[\nabla_\perp \left\{ \psi_{i,\perp}(\mathbf{r}'_\perp) \right\}; i q_{z,i} \psi_{i,\perp}(\mathbf{r}'_\perp) \right] \delta(\epsilon_f - \epsilon_i + \omega) = \\
&= \frac{2\hbar e^2}{L^2 \omega^2 m^2} \int d^3\mathbf{r} d^3\mathbf{r}' e^{i(z-z')(q_{z,f}-q_{z,i})} \delta(\epsilon_f - \epsilon_i + \omega) \psi_{f,\perp}(\mathbf{r}_\perp) \psi_{f,\perp}^*(\mathbf{r}'_\perp) \\
&\quad \times \left[\nabla_\perp \left\{ \psi_{i,\perp}^*(\mathbf{r}_\perp) \right\}; -i q_{z,i} \psi_{i,\perp}^*(\mathbf{r}_\perp) \right] \cdot \text{Im} \left[\hat{\mathbf{G}}(\mathbf{r}, \mathbf{r}', \omega) \right] \cdot \left[\nabla_\perp \left\{ \psi_{i,\perp}(\mathbf{r}'_\perp) \right\}; i q_{z,i} \psi_{i,\perp}(\mathbf{r}'_\perp) \right].
\end{aligned} \tag{1.22}$$

Now we will express the loss probability for a given energy (frequency ω). The time T it takes one electron to move along path of length L on the z axis with speed v is $T = L/v$. Since our previous expression describes the (time) rate of the transition of an electron from the well-defined initial state to a specific final state, to get the overall probability of the electron transitioning to any of the final states we will need to sum over all the possible final states and multiply the rate of transition by the electron-specimen interaction time (see above). From there we get the loss probability spectrum:

$$\Gamma(\omega) = \frac{L}{v} \sum_f \frac{d\Gamma_{i \rightarrow f}}{dt}. \tag{1.23}$$

The sum over all states can be replaced by integral over all possible final-state wave vectors. Below we split the sum into summation over the perpendicular component of wavevector and another summation (rewritten as integral) over the z -component of the electron's wavevector. We further need a prefactor $L/2\pi$ converting the wave vector $q_{z,f}$ to its corresponding frequency ϵ_f , resulting in

$$\Gamma(\omega) = \frac{L}{v} \sum_{f,\perp} \int dq_{z,f} \frac{L}{2\pi} \frac{d\Gamma_{i \rightarrow f}}{dt}. \tag{1.24}$$

We now combine Eqs. (1.24) with (1.22) and obtain

$$\begin{aligned}
\Gamma(\omega) &= \frac{\hbar e^2}{v \omega^2 \pi m^2} \int d^3\mathbf{r} d^3\mathbf{r}' \sum_{f,\perp} \int dq_{z,f} e^{i(z-z')(q_{z,f}-q_{z,i})} \delta(\epsilon_f - \epsilon_i + \omega) \psi_{f,\perp}(\mathbf{r}_\perp) \psi_{f,\perp}^*(\mathbf{r}'_\perp) \\
&\quad \times \left[\nabla_\perp \left\{ \psi_{i,\perp}^*(\mathbf{r}_\perp) \right\}; -i q_{z,i} \psi_{i,\perp}^*(\mathbf{r}_\perp) \right] \cdot \text{Im} \left[\hat{\mathbf{G}}(\mathbf{r}, \mathbf{r}', \omega) \right] \cdot \left[\nabla_\perp \left\{ \psi_{i,\perp}(\mathbf{r}'_\perp) \right\}; i q_{z,i} \psi_{i,\perp}(\mathbf{r}'_\perp) \right]
\end{aligned} \tag{1.25}$$

Let's focus on the innermost integral of the previous expression for now:

$$\int dq_{z,f} e^{i(z-z')(q_{z,f}-q_{z,i})} \delta(\epsilon_f - \epsilon_i + \omega).$$

Energy and momentum of a particle are closely related. If we write energy expressed in terms of momentum $p = \hbar q$ on one side of an equation and in terms of its frequency ϵ on the other side, we get

$$\frac{(\hbar q)^2}{2m} = \hbar \epsilon, \tag{1.26}$$

thus the frequency can be expressed as

$$\epsilon = \frac{\hbar q^2}{2m}. \quad (1.27)$$

We will now assume that most of the electron's energy is bound in the movement along the z axis. Thus we will be able to express all of the energy-related frequencies in terms of z components of wavevectors. In other words, we will use paraxial (or non-recoil) approximation. Because of the filtering property of the Dirac's delta δ , the result of the integral is the integrand in which we substitute for the integrated variable the value, in which the argument of δ is equal to zero. Using previous expression, we get

$$\begin{aligned} 0 &= \frac{\hbar q_f^2}{2m} - \frac{\hbar q_i^2}{2m} + \omega, \\ q_f &= q_i \sqrt{1 - \frac{2m}{\hbar q_i^2} \omega} \approx \\ &\approx q_i \left(1 - \frac{m}{\hbar q_i^2} \omega \right). \end{aligned} \quad (1.28)$$

The z subscripts were intentionally left out for clarity. In the last step we assumed that $\omega \ll \epsilon_i$ and the square root approximation rule (see A.1) was used. This is a very plausible step, since the swift electron loses typically only fraction of order lower than 10^{-3} of its initial energy interacting with the specimen originally in its ground state (i.e. not excited by other means) [8, p. 213].

Expanding the last term with momentum $\hbar q_i = p = mv$, we get

$$q_f = q_i \left(1 - \frac{\omega}{v q_i} \right). \quad (1.29)$$

Further, we substitute [from Eq. (1.27)] for $dq_{z,f} = d\epsilon_f m / \hbar q_{z,f} = d\epsilon_f / v$. Altogether we get

$$\int dq_{z,f} e^{i(z-z')(q_{z,f}-q_{z,i})} \delta(\epsilon_f - \epsilon_i + \omega) = \frac{1}{v} \exp\left(-i\omega \frac{z-z'}{v}\right). \quad (1.30)$$

By substituting this integral into Eq. (1.25) we get

$$\begin{aligned} \Gamma(\omega) &= \frac{\hbar e^2}{v^2 \omega^2 \pi m^2} \int d^3 \mathbf{r} d^3 \mathbf{r}' \exp\left(-i\omega \frac{z-z'}{v}\right) \sum_{f,\perp} \psi_{f,\perp}(\mathbf{r}_\perp) \psi_{f,\perp}^*(\mathbf{r}'_\perp) \\ &\quad \times \left[\nabla_\perp \{ \psi_{i,\perp}^*(\mathbf{r}_\perp) \}; -i q_{z,i} \psi_{i,\perp}^*(\mathbf{r}_\perp) \right] \cdot \text{Im} \left[\hat{\mathbf{G}}(\mathbf{r}, \mathbf{r}', \omega) \right] \cdot \left[\nabla_\perp \{ \psi_{i,\perp}(\mathbf{r}'_\perp) \}; i q_{z,i} \psi_{i,\perp}(\mathbf{r}'_\perp) \right] \end{aligned} \quad (1.31)$$

For further simplification, we define

$$\hat{\mathcal{G}}(\mathbf{r}_\perp, \mathbf{r}'_\perp, \omega) = \int dz dz' \exp\left(-i\omega \frac{z-z'}{v}\right) \text{Im} \left[\hat{\mathbf{G}}(\mathbf{r}, \mathbf{r}', \omega) \right] \quad (1.32)$$

and substitute this into the Eq. (1.31); we get

$$\begin{aligned} \Gamma(\omega) &= \frac{\hbar e^2}{v^2 \omega^2 \pi m^2} \int d^2 \mathbf{r}_\perp d^2 \mathbf{r}'_\perp \sum_{f,\perp} \psi_{f,\perp}(\mathbf{r}_\perp) \psi_{f,\perp}^*(\mathbf{r}'_\perp) \\ &\quad \times \left[\nabla_\perp \{ \psi_{i,\perp}^*(\mathbf{r}_\perp) \}; -i q_{z,i} \psi_{i,\perp}^*(\mathbf{r}_\perp) \right] \cdot \hat{\mathcal{G}}(\mathbf{r}_\perp, \mathbf{r}'_\perp, \omega) \cdot \left[\nabla_\perp \{ \psi_{i,\perp}(\mathbf{r}'_\perp) \}; i q_{z,i} \psi_{i,\perp}(\mathbf{r}'_\perp) \right]. \end{aligned} \quad (1.33)$$

For the sum in the last expression, we can again move from discrete to continuous domain. Now, it is time to decide, whether it will be best to work in Cartesian or in polar coordinates. This depends on the form of wave and the type of detector i.e. their symmetries. If the detector were square or the wave were of any arbitrary (radially non-symmetric) shape, we shall use Cartesian coordinates and integrate over the detector's q -space.

$$\sum_{f,\perp} \rightarrow \frac{A}{(2\pi)^2} \int dq_{f,x} \int dq_{f,y}. \quad (1.34)$$

As the basis for the space of wave functions ψ_{\perp} , we can then use a set of functions of the form

$$\psi_{\perp}^{(q_x, q_y)} = \frac{1}{\sqrt{A}} \exp [i(q_x x + q_y y)], \quad (1.35)$$

where A is a normalization constant.

The spectral loss function then becomes

$$\begin{aligned} \Gamma(\omega) = & \frac{\hbar e^2}{v^2 \omega^2 \pi m^2} \int dx dy dx' dy' \frac{A}{(2\pi)^2} \int dq_{f,x} e^{i q_{f,x}(x-x')} \int dq_{f,y} e^{i q_{f,y}(y-y')} \\ & [\nabla_{\perp} \{ \psi_{i,\perp}^*(x, y) \}; -i q_{z,i} \psi_{i,\perp}^*(x, y)] \cdot \hat{\mathcal{G}}(x, y, x', y', \omega) \cdot [\nabla_{\perp} \{ \psi_{i,\perp}(x', y') \}; i q_{z,i} \psi_{i,\perp}(x', y')]. \end{aligned} \quad (1.36)$$

If there exists an azimuthal symmetry in the problem, however, it might be better to use polar coordinates. In our case (when studying VEBs) it is convenient to use a basis of functions of form (1.19). These hold the vorticity of the beam naturally and can be expressed as

$$\psi_{f,\perp}(r, \phi) = \frac{1}{\sqrt{A}} e^{i l_f \phi} J_l(q_{f,r} r), \quad (1.37)$$

To move from discrete to continuous domain, we can write

$$\sum_{f,\perp} \rightarrow \frac{A}{(2\pi)^2} \int_0^{Q_c} q_{f,r} dq_{f,r} \int_0^{2\pi} dq_{f,\phi} \sum_{l_f} = \frac{A}{2\pi} \int_0^{Q_c} q_{f,r} dq_{f,r} \sum_{l_f}, \quad (1.38)$$

where we can evaluate the second integral since used basis functions are $q_{f,\phi}$ -independent.

When the OAM sorter is used, only one basis function corresponding to the concrete chosen l_f is then needed to describe the final state, and we can leave out the sum over all possible l_f s. Loss probability spectrum for the chosen l_f is then

$$\begin{aligned} \Gamma_{l_f}(\omega) = & \frac{\hbar e^2}{2\pi^2 v^2 \omega^2 m^2} \int d^2 \mathbf{r}_{\perp} d^2 \mathbf{r}'_{\perp} e^{i l_f (\phi - \phi')} \int_0^{Q_c} q_{f,r} dq_{f,r} J_l(q_{f,r} r) J_l(q_{f,r} r') \\ & \times [\nabla_{\perp} \{ \psi_{i,\perp}^*(\mathbf{r}_{\perp}) \}; -i q_{z,i} \psi_{i,\perp}^*(\mathbf{r}_{\perp})] \cdot \hat{\mathcal{G}}(\mathbf{r}_{\perp}, \mathbf{r}'_{\perp}, \omega) \cdot [\nabla_{\perp} \{ \psi_{i,\perp}(\mathbf{r}'_{\perp}) \}; i q_{z,i} \psi_{i,\perp}(\mathbf{r}'_{\perp})]. \end{aligned} \quad (1.39)$$

This is the final expression for the energy loss spectral function (EELSF).² It describes the probability density (upon range of photon frequencies ω) of electron losing energy $\hbar\omega$ if we know, that after interaction with the specimen the electron had left with final topological

²However, we do not use this exact expression to calculate our semianalytical spectra. See Sec. 2.1, precisely Eq. (2.18) for further explanation.

charge l_f . If more states with different topological charges from the set $\{l_f\}$ are needed, the spectral loss function for those states would be a simple sum

$$\Gamma_{\{l_f\}}(\omega) = \sum_{l \in \{l_f\}} \Gamma_l(\omega). \quad (1.40)$$

1.3 About Electron Energy Loss Spectroscopy

In the previous section, we derived an expression for the Electron Energy Loss Spectral Function (EELSF) of a swift electron impinging on a polarizable point-like particle. Now we briefly examine Electron Energy Loss Spectroscopy (EELS) as an experimental technique and focus on the low-energy part of the spectrum where optical excitations reside.

A moving relativistic electron acts as a broadband source of an oscillating evanescent electromagnetic field,[18] which can excite optical excitations in the specimen. In a form of photons with the frequency of the field, the specimen can then gain energy. The basic principle of EELS is the Law of conservation of energy. Instead of measuring energy gained by the specimen, we measure the energy lost by the electron. If we measure that the electron interacting with a specimen lost some defined energy $\hbar\omega$, we immediately know that the specimen must have gained the same amount of energy $\hbar\omega$ from the interaction. The result of an EELS measurement is electron energy loss spectrum (spectral function, EELSF) denoted Γ . This spectrum shows the probability density of a defined energy loss and if we integrate over a specific interval of energies (frequencies) we get the probability of electron losing (thus specimen gaining) the energy (frequency) from the chosen interval.

EELS is typically measured in STEMs. By scanning over the specimen, EELS maps the specimen by interaction in the near field. The spatial resolution is thus mainly limited by the span of the evanescent field produced by the electron. Thanks to the near-field character of the interaction, we are not bound to the radiative optical modes of the specimens. The fact that EELS maps all excitations is a big advantage in comparison to cathodoluminescence (CL) which accounts only for radiative modes, thus generally $\Gamma_{\text{EELS}} \geq \Gamma_{\text{CL}}$. García de Abajo and Kociak showed, [10] that in the case of geometries where translational invariance in the direction of the beam exists, the EELS spectrum is proportional to the local density of optical states (LDOS) enabling us to directly link EELS signal to a relevant optical quantity. For more general geometries this may not hold, however, in many cases it (at least qualitatively) does.

Thanks to the correlation with LDOS, EELS can be used to probe plasmons [5]. Nowadays even plasmon tomography is possible [18]. EELS can be angle-resolved which enables us to study structures with translational symmetries in the inverse space rather than in the real. The energy resolution in some setups has already lowered under 10 meV and we are able to analyze energies > 30 meV, which enables us to study even phononic and vibrational excitations. Such high energy resolution was gained mainly thanks to the reduction of zero-loss peak (which is the signal from electrons which did not interact with the specimen at all) and improvements in monochromator designs.

To model interaction with optical excitations in a realistic sample, one usually has to numerically solve Maxwell's equations. Several methods are known. One of them is Boundary Element Method (BEM), which is further discussed in Ch. 3. In some cases, as is ours for the point-like particle in Ch. 2, we can bypass the numerical solution.

When the specimen is excited before (or together) with the interaction with the specimen, e.g. thermally or by external optical stimulation, it can also give the energy to (not take it

from) the electron. When this phenomenon is measured in spectra, we talk about Electron Energy Gain Spectroscopy (EEGS)

Temporal information about the interaction with the specimen can be gained from Fourier analysis of the measured data or by employing ultrafast TEM setups.

Structured beams in EELS

As we discussed in the Sec. 1.1 the wave functions of electrons can be tailored in multifarious ways (for example with programmable phase plates (PPPs)) both in amplitude and phase. The control over the beam shape introduces a new degree of freedom which can be used to study more phenomena in a more simple and faster measurement or even open new fields of study for example in the study of magnetic structures or chiral substances of materials which are very common in nature. Beams structured in spatial or temporal domains can be viewed as "quantum probes" which can reveal all kinds of new information about specimen since after the interaction the electron's state is entangled with the specimen's. This enables us to analyze the state of electrons and gain information about the state of specimens. This can open new fields in microscopy. Last but not least, the use of structured electron beams can possibly reduce the need for conventional electron optics (e.g., correctors) and reduce the complexity of electron microscopes columns. Thus TEMs could become smaller and a "tabletop" solution could become possible.

Chapter 2

Semi-Analytical Model of VEB's Interaction with a Chiral Point Object

2.1 Green's Response Tensor

In this section, we will discuss Green's response tensor needed for the evaluation of the EEL spectral function derived in Sec. 1.2.

For the next couple of paragraphs, we roughly follow [17]. Helmholtz equation for electromagnetic field in the domain of frequencies ω with corresponding wavenumber $k = \omega/c$ (where c is the speed of light) in a vacuum with the Lorenz gauge can be written in the following form for 4-potential A^i (thus for classical vector and scalar potentials) and 4-current J^i as

$$\left[\nabla^2 + k^2\right] A^i = -\mu_0 J^i. \quad (2.1)$$

Let us focus now on any one component. Assuming the charge density (or one particular component of current density) to be concentrated in one concrete (source) point \mathbf{r}' so that the total charge (current) is unit, we can rewrite the previous expression for any (field) point \mathbf{r} in space using Dirac's delta as

$$\left[\nabla^2 + k^2\right] G_0(\mathbf{r}, \mathbf{r}') = -\delta(\mathbf{r} - \mathbf{r}'), \quad (2.2)$$

where $G_0(\mathbf{r}, \mathbf{r}')$ is some function. Since the Helmholtz operator is linear, there exists (in general) an inverse operator (traditionally called Green's operator) which acts as a response operator on the unit impulse. If this operator is known, we can then find the response for any possible impulse. In our case we can find the potential field $A^i(\mathbf{r})$ in any point in space for any possible current density field $J^i(\mathbf{r})$ as

$$A^i(\mathbf{r}) = \underbrace{\int d^3\mathbf{r}' \mu_0 G_0(\mathbf{r}, \mathbf{r}') J^i(\mathbf{r}')}_{\text{mentioned linear operator}}, \quad (2.3)$$

where we have underbraced the mentioned linear operator.

A solution for the 3D Helmholtz equation (2.2) can be found in the form

$$G_0(\mathbf{r}, \mathbf{r}') = \frac{\exp(i k |\mathbf{r} - \mathbf{r}'|)}{4\pi |\mathbf{r} - \mathbf{r}'|}. \quad (2.4)$$

The function $G_0(\mathbf{r}, \mathbf{r}')$ is known as scalar vacuum Green's function. We can see that the expression is dependent only on the difference between \mathbf{r} and \mathbf{r}' , thus it is possible to write $G_0(\mathbf{r}, \mathbf{r}') = G_0(\mathbf{r} - \mathbf{r}')$.

Similarly, the Green's operator can be found for electric \mathbf{E} and magnetic \mathbf{B} fields. Since those are 3-component vector quantities the Green's operator must be a tensor of rank 3.

$$\mathbf{E}(\mathbf{r}) = \frac{i}{\omega} \int d^3\mathbf{r}' \hat{\mathbf{G}}_{\text{EE}}(\mathbf{r}, \mathbf{r}') \cdot \mathbf{J}(\mathbf{r}'), \quad (2.5)$$

$$\mathbf{B}(\mathbf{r}) = \frac{i}{\omega} \int d^3\mathbf{r}' \hat{\mathbf{G}}_{\text{ME}}(\mathbf{r}, \mathbf{r}') \cdot \mathbf{J}(\mathbf{r}'). \quad (2.6)$$

The current density \mathbf{J} can be further calculated from dipole moment \mathbf{p} as

$$\mathbf{J}(\mathbf{r}') = -i\omega \mathbf{p} \delta(\mathbf{r}' - \mathbf{r}_0), \quad (2.7)$$

where \mathbf{r}_0 is the position of the dipole.

The Green's dyadic electro-electric function $\hat{\mathbf{G}}_{\text{EE}}$ can be calculated from the scalar vacuum Green's function G_0 as

$$\hat{\mathbf{G}}_{\text{EE}}(\mathbf{r}, \mathbf{r}') = \frac{1}{\varepsilon_0} [k^2 \hat{\mathbf{1}} + \nabla' \otimes \nabla'] G_0(\mathbf{r}, \mathbf{r}'), \quad (2.8)$$

where $\hat{\mathbf{1}}$ is unit operator, ∇' is the nabla operator in respect to primed (source) position vector \mathbf{r}' and \otimes stands for tensor product. The Green's dyadic electro-magnetic function $\hat{\mathbf{G}}_{\text{ME}}$ is then

$$\hat{\mathbf{G}}_{\text{ME}}(\mathbf{r}, \mathbf{r}') = \frac{1}{i\omega} \nabla' \times \hat{\mathbf{G}}_{\text{EE}}(\mathbf{r}, \mathbf{r}'). \quad (2.9)$$

It describes the magnetic field induced by an electrical current (dipole).

From the symmetry of Maxwell's equations, [15] it can be shown that Green's magneto-magnetic tensor fulfils

$$\hat{\mathbf{G}}_{\text{MM}} = \hat{\mathbf{G}}_{\text{EE}} \quad (2.10)$$

and Green's magneto-electric tensor can be found as

$$\hat{\mathbf{G}}_{\text{EM}} = -\hat{\mathbf{G}}_{\text{ME}}. \quad (2.11)$$

In Eq. (1.32) we defined (following Ref. [15]) a Green's response tensor integrated along z axes. To fully construct it, we will define

$$\begin{aligned} \hat{\mathbf{G}}_{\text{EE}}^{\text{int}}(\mathbf{r}, \mathbf{r}') &= \int dz dz' \exp\left(-i\omega \frac{z-z'}{v}\right) \hat{\mathbf{G}}_{\text{EE}} = \\ &= \frac{1}{2\pi\varepsilon_0} (k^2 \hat{\mathbf{1}} + \nabla' \otimes \nabla') \left[e^{i\omega \frac{z_p}{v}} K_0\left(\frac{\omega |\mathbf{r}_\perp - \mathbf{r}'_\perp|^2}{v \gamma_L}\right) \right], \end{aligned} \quad (2.12)$$

where K_0 is modified Bessel's function of order 0, $\gamma_L = 1/\sqrt{1-v^2/c^2}$ is Lorentz factor.

Thanks to the linearity of differential operators used in derivation of dyadic functions from vacuum Green function, the previously stated relations between different Green's tensors are retained for their integrated forms:

$$\hat{\mathbf{G}}_{\text{EM}}^{\text{int}}(\mathbf{r}, \mathbf{r}') = -\frac{1}{i k c} \nabla' \times \hat{\mathbf{G}}_{\text{EE}}^{\text{int}}(\mathbf{r}, \mathbf{r}'), \quad (2.13)$$

$$\hat{\mathbf{G}}_{\text{MM}}^{\text{int}} = \hat{\mathbf{G}}_{\text{EE}}^{\text{int}}, \quad (2.14)$$

2.1. GREEN'S RESPONSE TENSOR

and

$$\hat{\mathbf{G}}_{\text{ME}}^{\text{int}} = -\hat{\mathbf{G}}_{\text{EM}}^{\text{int}}. \quad (2.15)$$

The electron moving in the microscope column generates an electric and magnetic field around the specimen. This is described by Green's electro-electric and electro-magnetic tensors.

This field then acts on the specimen and can induce electric \mathbf{p} or magnetic μ dipole on it. Assuming the specimen is small enough so the field around it is homogeneous we can describe it by simple polarizability tensors:

$$\begin{array}{ll} \text{electro-electric} & \mathbf{E} \rightarrow \mathbf{p} \quad \hat{\alpha}_{\text{EE}} , \\ \text{electro-magnetic} & \mathbf{E} \rightarrow \mu \quad \hat{\alpha}_{\text{ME}} , \\ \text{magneto-electric} & \mathbf{H} \rightarrow \mathbf{p} \quad \hat{\alpha}_{\text{EM}} , \\ \text{electro-magnetic} & \mathbf{H} \rightarrow \mu \quad \hat{\alpha}_{\text{MM}} . \end{array}$$

Again, thanks to the symmetry between electric and magnetic fields, in reciprocal materials we can write

$$\hat{\alpha}_{\text{ME}} = -\hat{\alpha}_{\text{EM}}^T \quad (2.16)$$

The induced electric (magnetic) dipole creates its own electric and magnetic field, which is captured, again, by Green's electro-electric and electro-magnetic (magneto-electric and magneto-magnetic) tensors.

It is essential to mention that if the specimen were polarizable in the crossed electro-magnetic terms $\hat{\alpha}_{\text{EM}}$ and $\hat{\alpha}_{\text{ME}}$, it must always be polarizable in the electric $\hat{\alpha}_{\text{EE}}$ and magnetic $\hat{\alpha}_{\text{MM}}$ terms. [2]

The induced magnetic field does not change the energy of the electron. We can also assume that the trajectory of the electron is almost unchanged by the magnetic field produced by the specimen. This means that we can neglect magnetic forces acting on the electron in our computations relating EELS. To capture the whole interaction of the electron with the specimen, we then define Green's response tensor

$$\check{\mathcal{G}}(\mathbf{r}, \mathbf{r}', \omega) = \check{\mathcal{G}}_{\text{EE}}(\mathbf{r}, \mathbf{r}', \omega) = \hat{\mathbf{G}}_{\text{E}i}^{\text{int}}(\mathbf{r}, \mathbf{r}_p, \omega) \cdot \hat{\alpha}_{ij}(\omega) \cdot \hat{\mathbf{G}}_{j\text{E}}^{\text{int}}(\mathbf{r}_p, \mathbf{r}', \omega), \quad (2.17)$$

where we have used Einstein summation rule (ESR) through indices $i, j \in \{\text{E}, \text{M}\}$ and \mathbf{r}_p is the position of the studied particle (specimen). This tensor is in fact only electro-electric, as we have captured by the lower indices EE. However, since we don't need the magnetic ones we will omit the lower indices straight away. This is not yet the Green's response tensor defined in Eq. (2.17). However we were able to find the green response operator "without the imaginary part function" (compare Eqs. (1.32) and (2.12)). In the Eq. (1.39) the imaginary part is still inside the integrand. Fortunately, it can be pulled out [8] in front of the integral and EELSF can be calculated as

$$\begin{aligned} \Gamma_{l_i \rightarrow l_f}(\omega) = & \frac{\hbar e^2}{2\pi^2 v^2 \omega^2 m^2} \text{Im} \left\{ \int d^2\mathbf{r}_\perp d^2\mathbf{r}'_\perp e^{i l_f(\phi - \phi')} \int_0^{Q_c} q_{f,r} dq_{f,r} J_l(q_{f,r} r) J_l(q_{f,r} r') \right. \\ & \left. \times \left[\nabla_\perp \left\{ \psi_{i,\perp}^*(\mathbf{r}_\perp) \right\}; -i q_{z,i} \psi_{i,\perp}^*(\mathbf{r}_\perp) \right] \cdot \check{\mathcal{G}}(\mathbf{r}_\perp, \mathbf{r}'_\perp, \omega) \cdot \left[\nabla_\perp \left\{ \psi_{i,\perp}(\mathbf{r}'_\perp) \right\}; i q_{z,i} \psi_{i,\perp}(\mathbf{r}'_\perp) \right] \right\}. \end{aligned} \quad (2.18)$$

To grasp the interaction intuitively, a diagram of the interaction is shown in Fig. 2.1. Let's focus on this Figure now and explain intuitively what is happening. As we have already

mentioned, a swift electron is a source of optical excitation thanks to its evanescent field. When a point-like particle is placed in the vicinity of the beam, it feels the field. We have described the particle by four polarizability tensors. Two of them are "pure", $\hat{\alpha}_{EE}$ and $\hat{\alpha}_{MM}$, and two of them are "crossed". In our setup, we have another degree of freedom – the distance between the specimen and the center of the vortex.

The pure terms account for achiral (or non-chiral) modes excited on the particle. The crossed terms are at play if the particle is chiral in nature (by material or structure). On such particle, chiral modes can be excited.

Any modes excited create their own field which acts back on the electron. This is how the electron loses its energy. After the interaction, the electron is in a superposition of all possible final states.

If not only the specimen is chiral but the electron impinging on it too, the symmetry breaks and dichroism emerges. In this context, dichroism is the effect of different responses to qualitatively opposite impulses, the difference between response on right-hand vs left-hand vortex or, with the same initial topological charge l , the difference between positive $+\Delta l$ vs negative $-\Delta l$ change of topological charge in the interaction.

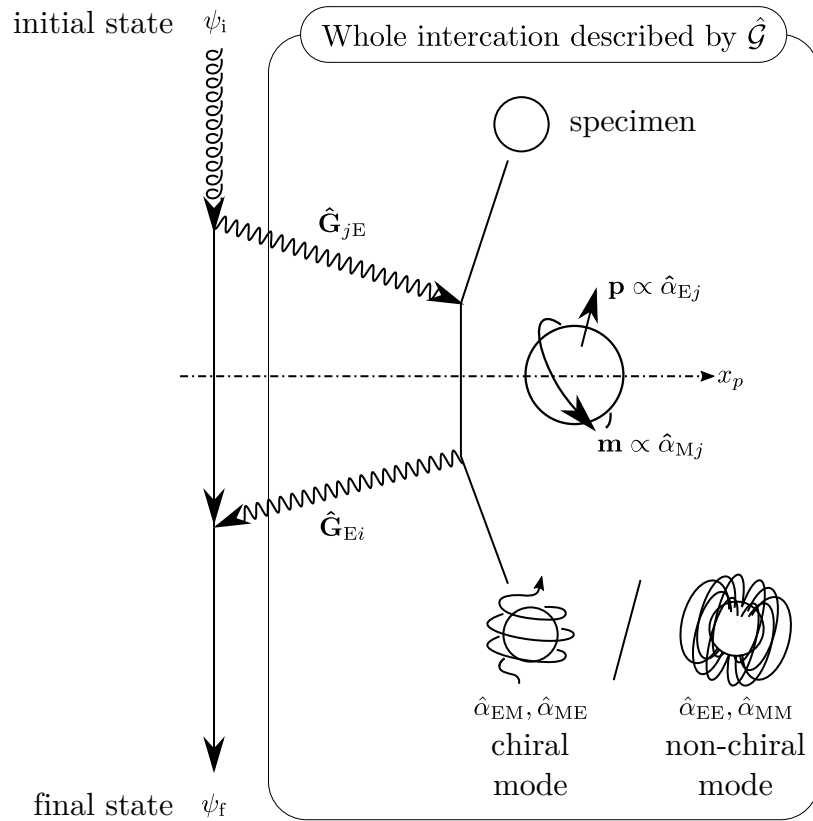


Figure 2.1: Diagram of the interaction of an electron with the specimen.

2.1.1 Drude Model for Relative Permittivity

Frequency-dependent relative permittivities (dielectric functions) are usually tabulated. Some metals are well characterized by the Drude free electron model which yields the relative permittivity

$$\varepsilon(\omega) = 1 - \frac{\omega_p^2}{\omega^2 + i\gamma\omega}, \quad (2.19)$$

where ω_p is the bulk plasmon frequency of studied metal and γ is a small phenomenological relaxation rate which accounts for the dampening of plasma oscillation in the metal. In our calculations we used the values $\hbar\omega_p = 9.1$ eV and $\hbar\gamma = 0.15$ eV [8].

2.1.2 Polarizability Tensor of a Sphere

Thanks to the total symmetry of a sphere, the electric polarizability of a spherical metallic particle with radius a and relative permittivity $\varepsilon(\omega)$ can be described by a scalar function $\alpha(\omega)$ as [2]

$$\alpha(\omega) = 4\pi\varepsilon_0 \frac{3c^3}{2\omega^3} \frac{-j_1(\rho_0) [\rho_1 j_1(\rho_1)]' + \varepsilon(\omega) j_1(\rho_1) [\rho_0 j_1(\rho_0)]'}{h_1^{(+)}(\rho_0) [\rho_1 j_1(\rho_1)]' - \varepsilon(\omega) j_1(\rho_1) [\rho_0 h_1^{(+)}(\rho_0)]'}, \quad (2.20)$$

where $j_1(x) = \sin(x)/x^2 - \cos(x)/x$ and $h_1^{(+)}(x) = (1/x^2 - i/x) \exp(ix)$ are spherical Bessel and Hankel functions, respectively, prime stands for differentiation with respect to the argument and $\rho_0 = \omega a/c$ and $\rho_1 = \sqrt{\varepsilon(\omega)} \rho_0$. Said expression was used to gain realistic polarizability in our calculations, where we used universally the value for radius $a = 5$ nm. Throughout our calculations we assumed diagonal polarizability tensors with equal values in each axis so that $\hat{\alpha}(\omega) = \alpha(\omega) \cdot \hat{\mathbf{1}}$. More complicated (non-diagonal) tensor would work too. In Fig. 2.2 we plotted the scalar polarizability of a sphere for the stated parameters.

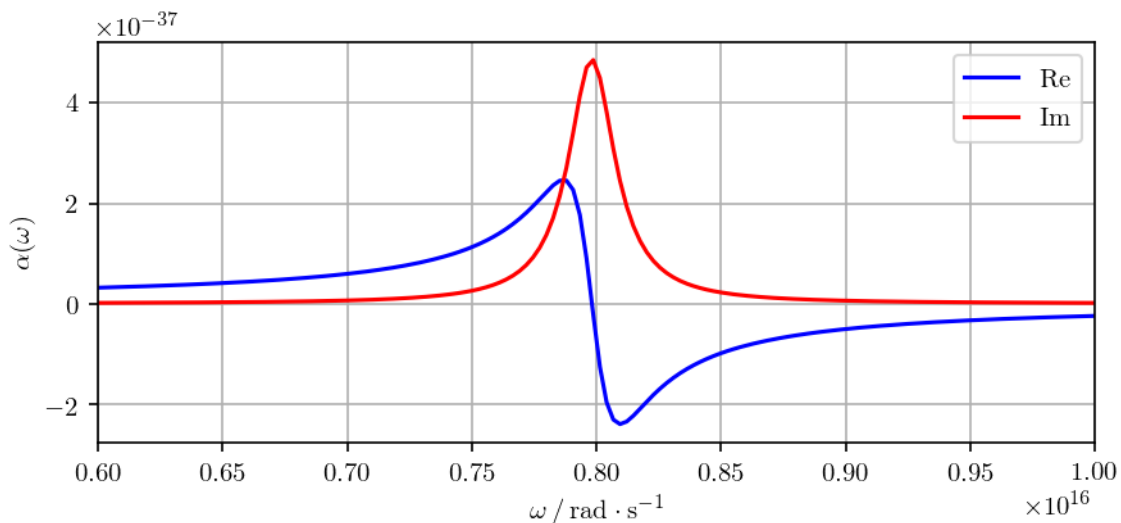


Figure 2.2: Scalar polarizability of metallic sphere.

2.2 Implementation

This section describes the implementation of calculations. After the derivation of expression for EELSF in Sec. 1.2 and derivation of Green's response tensor in Sec. 2.1 we could implement those into a computer program to calculate the spectra. We have chosen programming language PYTHON for the implementation since it is open-source and there exists a great number of libraries to use. It is well human-readable language and it is fast and easy to write. The calculation speed is not the best but it was sufficient for our purpose. The support for scientific calculations in libraries is also very good. Libraries we have used are: NUMPY, SCIPY, SYMPY, MATPLOTLIB and PLOTLY.

Now we shall explain how the calculation was implemented. We can rewrite the last expression for the EEL spectral function gamma (2.18) in the following form

$$\Gamma_{lf}(\omega) = \mathcal{J}(v, \omega) \int d^2\mathbf{r}_\perp d^2\mathbf{r}'_\perp \mathcal{Q}(\mathbf{r}, \mathbf{r}') \mathcal{K}(\mathbf{r}_\perp, \mathbf{r}'_\perp, \omega, v, \psi_i), \quad (2.21)$$

where

$$\mathcal{J} = \frac{\hbar e^2}{2\pi^2 v \omega^2 m^2} \quad (2.22)$$

is the prefactor, or "Jack function";

$$\mathcal{Q} = e^{i l_f(\phi - \phi')} \int_0^{Q_c} q_{f,r} dq_{f,r} J_l(q_{f,r} r) J_l(q_{f,r} r') \quad (2.23)$$

called "the Queen function", holds the radial profile of final vortex states and the interaction change of topological charge; and

$$\mathcal{K} = \left[\nabla_\perp \left\{ \psi_{i,\perp}^*(\mathbf{r}_\perp) \right\}; -i q_{z,i} \psi_{i,\perp}^*(\mathbf{r}_\perp) \right] \cdot \check{\mathcal{G}}(\mathbf{r}_\perp, \mathbf{r}'_\perp, \omega) \cdot \left[\nabla_\perp \left\{ \psi_{i,\perp}(\mathbf{r}'_\perp) \right\}; i q_{z,i} \psi_{i,\perp}(\mathbf{r}'_\perp) \right] \quad (2.24)$$

called "the King function" holds the initial wave functions of vortex and can be thought of as the main interaction part of the EELSF. For great part of the calculation the King and the Queen were treated separately and the Jack (as it is only a prefactor) was introduced in the end.

Both King and Queen were held in the memory of the computer as NUMPY arrays of numbers. The calculation (numerical integration of the computed 4D array) had to be performed for each point in the frequency ω domain. Fortunately, the Queen is not ω -dependent so in order to save computational time we have preevaluated the Queen for the calculation of whole spectrum with set parameters (such are topological charge, electron energy or speed) and only the King was recalculated for each ω -point.

To set up the computation parameters such are the number of points in space needed or the spatial range, we rendered several plots of initial wave functions, Kings and Queens before running the scripts. We also ran a convergence test for the number of space points. To get a reasonable compromise between calculation accuracy and computation speed we settled on 20 nm–30 nm wide field with 50 space points in each of four dimensions (x, y, x', y'). That is 6 250 000 points in total. These computation parameters are well compatible with set parameters of the electron beam with energy 60 keV corresponding to speed 0.446 c . We have assumed the beam to have lateral spread of 20 mrad.

Occasionally, when the mesh of our space coincides in some point with the position of the point-like specimen, NaN (Not a Number) values appear in our fields. Singularities are at these points and the values around them tend to diverge to $\pm\infty$ and PYTHON handles

them as NaNs. This is a problem in numerical integration so we had to use the function `numpy.nansum()` which ignores NaNs and assumes 0 instead of them. These singularities are non-physical and would be avoided when going beyond the point-particle model so this step should not break physics.

We have already mentioned that if the particle is polarizable in the crossed way – electrically (magnetically) by magnetic (electric) field, it must always be polarizable in the ”pure” way – electrically by electric and magnetically by magnetic field. Thanks to the linearity of Eq. (2.17), individual contributions from different types of polarizabilities can be calculated separately and we can get the final EELSF as a simple sum of contributions. Dichroism then arises only from the crossed electric-magnetic terms. To study the dichroism, it is thus convenient to calculate and study the dichroic contribution separately, as we will show later in the Sec. 2.3. We can write this into an equation.

$$\Gamma = \Gamma_{EE} + \Gamma_{EM} + \Gamma_{ME} + \Gamma_{MM}, \quad (2.25)$$

where by the indices EE, EM, ME and MM we denote the component of Γ corresponding to the contribution from polarizability tensors $\hat{\alpha}_{EE}$, $\hat{\alpha}_{EM}$, $\hat{\alpha}_{ME}$ and $\hat{\alpha}_{MM}$ respectively. Since $\hat{\alpha}_{EM} = -\hat{\alpha}_{ME}^T$, $\Gamma_{EM} = \Gamma_{ME}$. Thus, if we denote the dichroic component of spectrum $\Gamma_D = 2\Gamma_{EM}$, we can write

$$\Gamma = \Gamma_{EE} + 2\Gamma_{EM} + \Gamma_{MM} = \Gamma_{EE} + \Gamma_D + \Gamma_{MM}. \quad (2.26)$$

In the following section Results we present only Γ_{EE} and Γ_{EM} .

2.3 Results

In the last section of this chapter, we present our results in the form of computed spectra. There are two sets of spectra. Spectra for electro-electric polarizability and spectra for electro-magnetic polarizability. As we explained above, the presented spectra are only Γ_{EE} and Γ_{EM} contributions. Γ_{ME} would be exactly the same as Γ_{EM} , as we mentioned, and Γ_{MM} would have the same shape as Γ_{EE} but would be differently scaled. We do not include the “full” spectra since they would not give any new information and they would look (at first and also second glance) the same as “pure” electro-electric spectra). We are studying the spectra only semi-quantitatively. They are consistent with each other but not properly scaled in absolute value and are featured in arbitrary units (arb. u.). Thus we can compare the values between the spectra in relative measures. When comparing the dichroic spectra to the electro-electric spectra, one needs to have in mind that the scaling between them should reflect the real scaling between electro-electric and cross polarizabilities in the real specimen. In our calculation, we assumed polarizabilities of the same magnitude for crossed and electro-electric polarizabilities in the form of a diagonal tensor with equal elements (effectively scalar polarizability of a metal sphere). All conclusions are due to the facts stated above only qualitative.

In the following figures, we mostly keep the following conventions. 1) The colour of the line encodes the information about the initial topological charge l_i and its change to the final topological charge l_f . 2) The “density” (dashes, or dots) of the line is lower as the specimen is further away from the center of the vortex.

Dichroism intensity. In the descriptions of dichroic spectra we will use the term “dichroic intensity” or “intensity of dichroism”. By these terms we mean the relative intensity of dichroic spectrum extrema in comparison to other dichroic spectra or to the non-dichroic (main, electro-electric) signal. An important aspect of this term as we use it is that dichroism intensity “has a sign”. It is not important what the actual sign is, however, it is important when the profile of the dichroic spectrum flips over the zero and changes the sign. This means, as we will explain later, that instead of the “right-handed” vortex, the particle can “feel” the vortex as if it was “left-handed” and vice versa. If we say that the dichroic intensity is lower, we mean that the extreme values of the spectrum are smaller in absolute value.

The first spectra are presented in Fig. 2.3. In them, we can see standard (non-dichroic) Γ_{EE} contributions of EELSFs. In this particular graph, spectra for topological charge transitions from $l_i = 0 \rightarrow l_f = \pm 1$ are studied. It can be seen that all spectra approximately follow the shape of Lorentz functions, but reach different intensities. Note that in the non-crossed contributions we never see any difference between the excitation by right-handed and left-handed vortices, or in the spectra calculated for opposite topological charge transitions. This is confirmed also in Fig. 2.4 where we compare spectra gained for different specimen positions when the topological charge changes from ± 1 to ∓ 1 . Note that the curves reflect the shape of the imaginary part of assumed polarizability (see Fig. 2.2). In both figures mentioned in this paragraph, the dependence of the signal on the distance between the vortex center and the specimen is captured. More interesting results can be seen in Fig. 2.4, where the overall intensity first increases, it is maximal for $x_p = 1.5$ nm and then starts decreasing. This is probably related to hitting the “sweet spot” corresponding to the maximum of the VEB’s radial profile by the specimen. In both cases, we can also observe that when the specimen is positioned exactly at the axis of the vortex beam, the resulting signal is two orders of magnitude weaker.

In Figs. 2.5 – 2.8 we plot the Γ_{EM} components of EELSF, which are essentially the

dichroic spectra. Note that the profile corresponds to the real part of the polarizability (see Fig. 2.2).

Fig. 2.5 shows dichroic spectra for vortices of non-changing topological charges $+1$ and -1 for different positions of the specimen with respect to the vortex beam axis. The most important thing to notice is that the response to the left-handed vortex is opposite to the response to the right-handed vortex (compare blue and red lines). Very similar spectra for transition $l_i = 0 \rightarrow l_f = \pm 1$ are shown in Fig. 2.7. Here, the response is a little bit weaker. This is probably caused mostly by the fact that the change of topological charge is less probable than it staying the same.

The zero topological charge $l = 0$ is privileged over others since the wave function of a vortex is non-zero in the center of the vortex only in this case and the OAM of such VEB is 0. There is then no phase singularity and the problem is more symmetric. This can lead to the disappearance of dichroism. See Fig. 2.6. Interesting things happen also when comparing spectra with topological charge transition symmetric around zero (i. e. from $+l$ to $-l$ or vice versa). In this case, the system can be sufficiently symmetric too and the dichroism does not emerge either. This happened in spectra in Fig. 2.8 when the specimen was placed in the center of the VEB.

The most important conclusion based on our results is that the dependence of dichroism intensity on the position of the specimen relative to the center of the vortex is not trivial. See Figs. 2.8 and 2.9. To gain an intuitive understanding of what is happening, take a look at the schematics in Fig. 2.10. As we move the specimen away from the center of the vortex, the dichroic intensity first gradually increases as we move away from the center of the vortex, where it was (due to the symmetry of the problem) zero. From the maximum, as we go further away from the center, the dichroic intensity goes again to zero and even flips over to negative values. Again we reach an extremity and then the dichroic response is weakening again. This essentially means that the vortex probing the particle can see it in completely opposite (in the sense of right- vs. left-handed) manner. The proper knowledge about the spatial extent of the VEB and its exact position with respect to the specimen is thus essential to make any conclusions about the measured dichroic response. Ideally, the measurement in this setup with a point-like particle shall be performed multiple times so that the vortex is aimed at different spots (with different distances between vortex center and the specimen) around the particle. We got similar results for the “macroscopic” (in the sense of non-point-like) chiral nanostructure in Ch. 3.

All in all, we can conclude that the problematics of dichroic response to a polarizable point-like particle is multivariate and it is hard to formulate some general truths. There are (at least but not only) the initial topological charge magnitude and sign, the change of the topological charge (with respect to its magnitude), and the distance between the center of the vortex and the specimen at play. In addition, we have to consider parameters of vortex-forming electron optics as well as the collection geometry at the detector. It is possible to gain some intuition but a model should be made for every considered scenario.

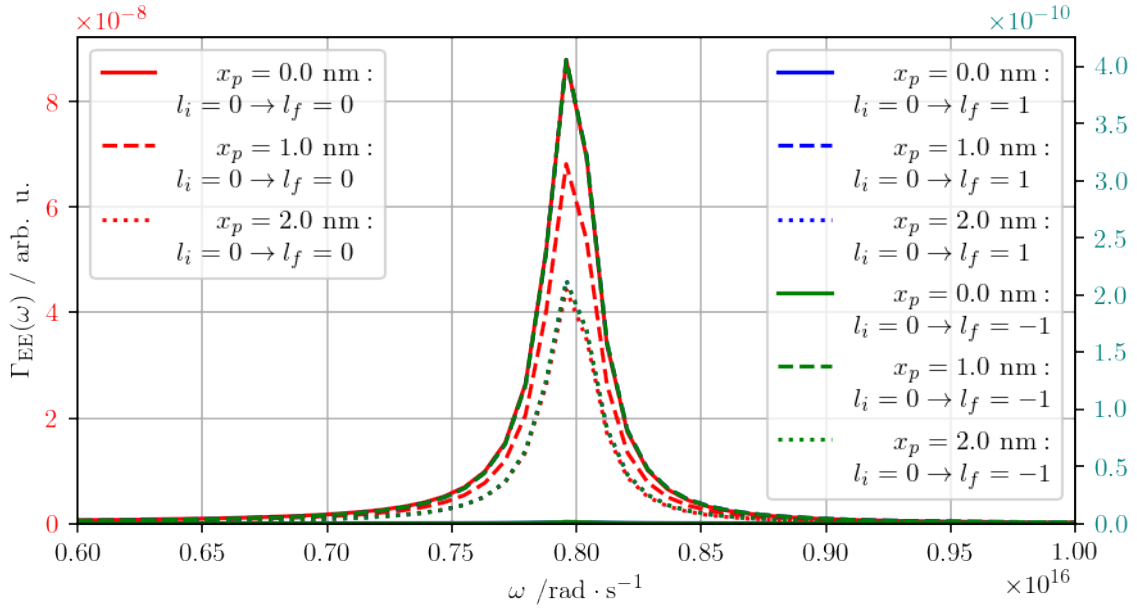


Figure 2.3: Comparison of electro-electric EELS spectra when the initial topological charge $l_i = 0$ does not change (red) vs changes to the final state $l_f = 1$ (blue) or $l_f = -1$ (green). Note that the blue and green spectra are differently scaled (on the right) than the red spectra and their magnitude is around two orders of magnitude higher. Green and Blue spectra for $x_p = 0$ are even another two orders of magnitude lower (so they look like straight lines at first glance). All blue lines are hidden under corresponding green.

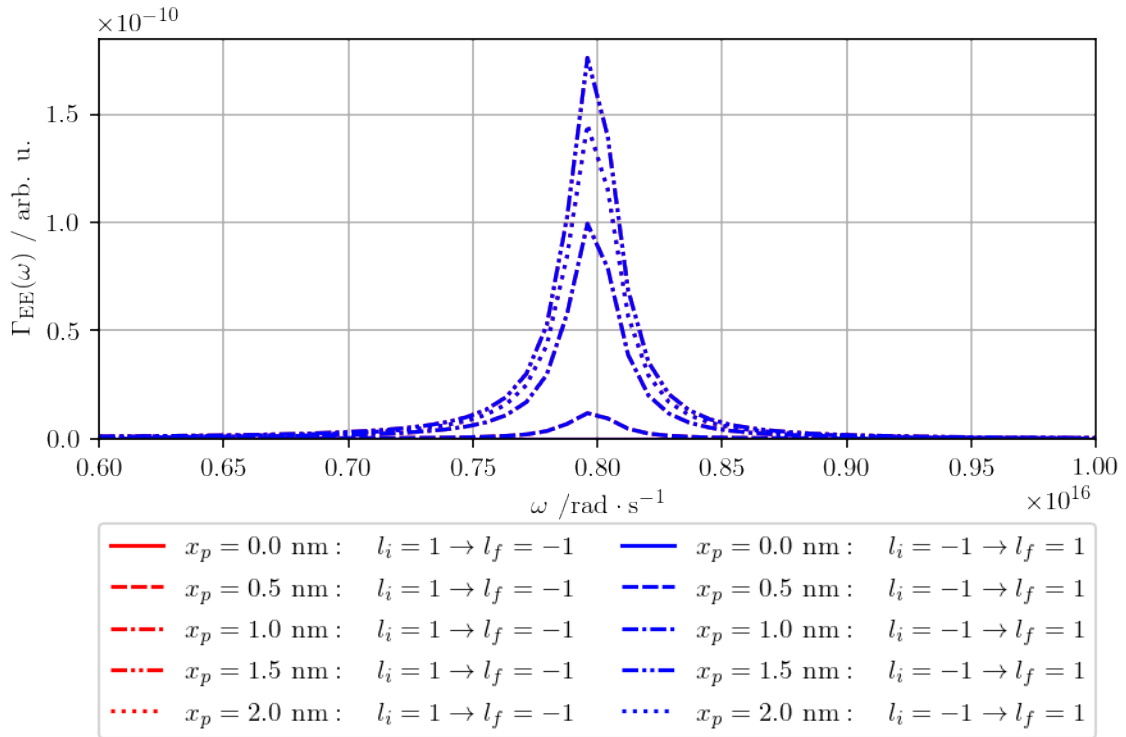


Figure 2.4: Comparison of transitions between topological charges from $l_i = -1$ to $l_f = 1$ and vice versa for different positions of specimen. All red lines are hidden under corresponding blue.

2.3. RESULTS

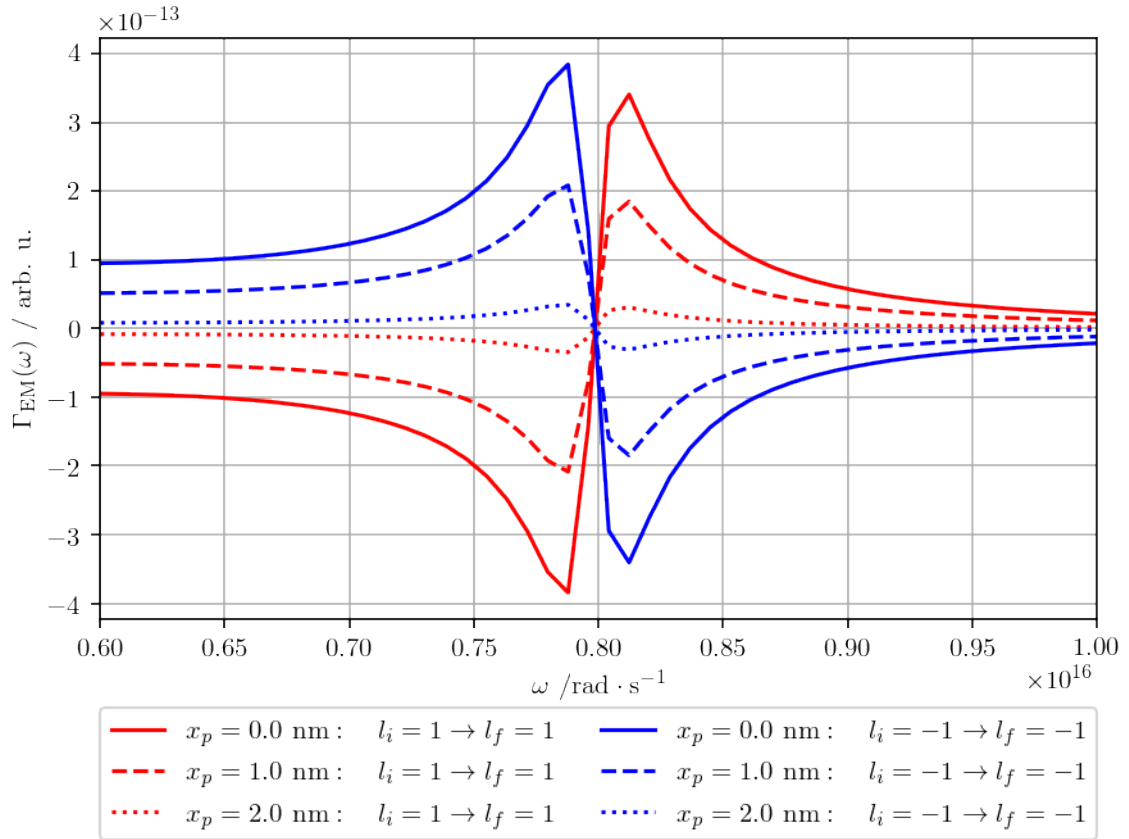


Figure 2.5: Dichroic spectra for non-changing topological charge $l_i = l_f = \pm 1$. Here in contrast to Fig. 2.6 the symmetry has been broken and dichroism emerges.

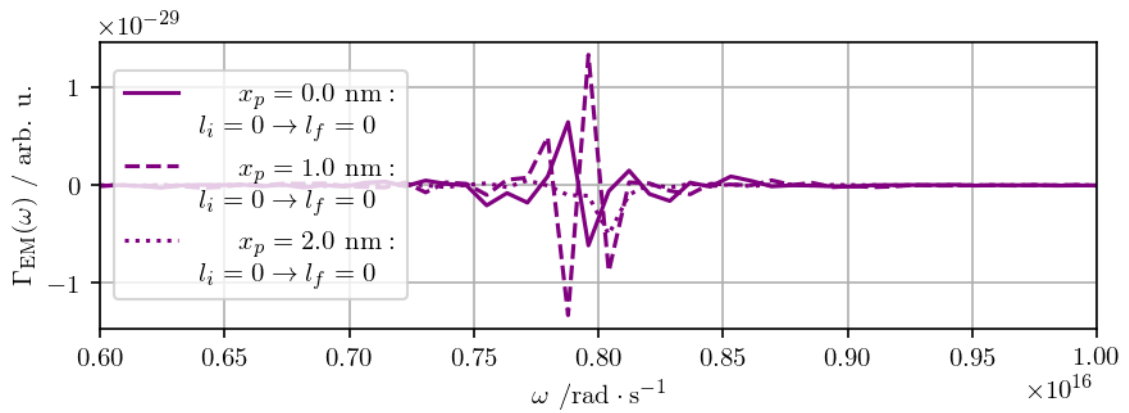


Figure 2.6: (Non)dichroic spectra for non-changing zero topological charge. The symmetry has not been broken so there is no dichroic response and we see only numerical noise.

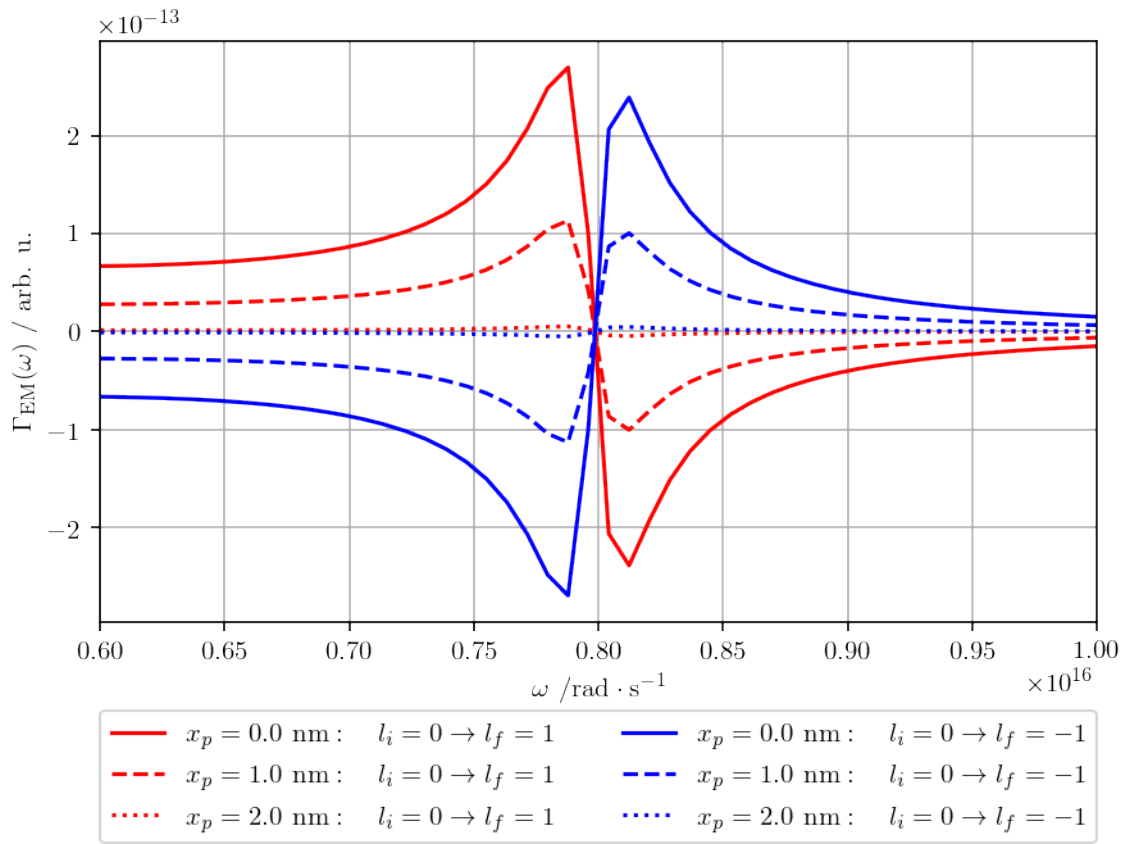


Figure 2.7: The dichroic response to the transition of topological charge from 0 to ± 1 for different distances of the specimen from the vortex center.

2.3. RESULTS

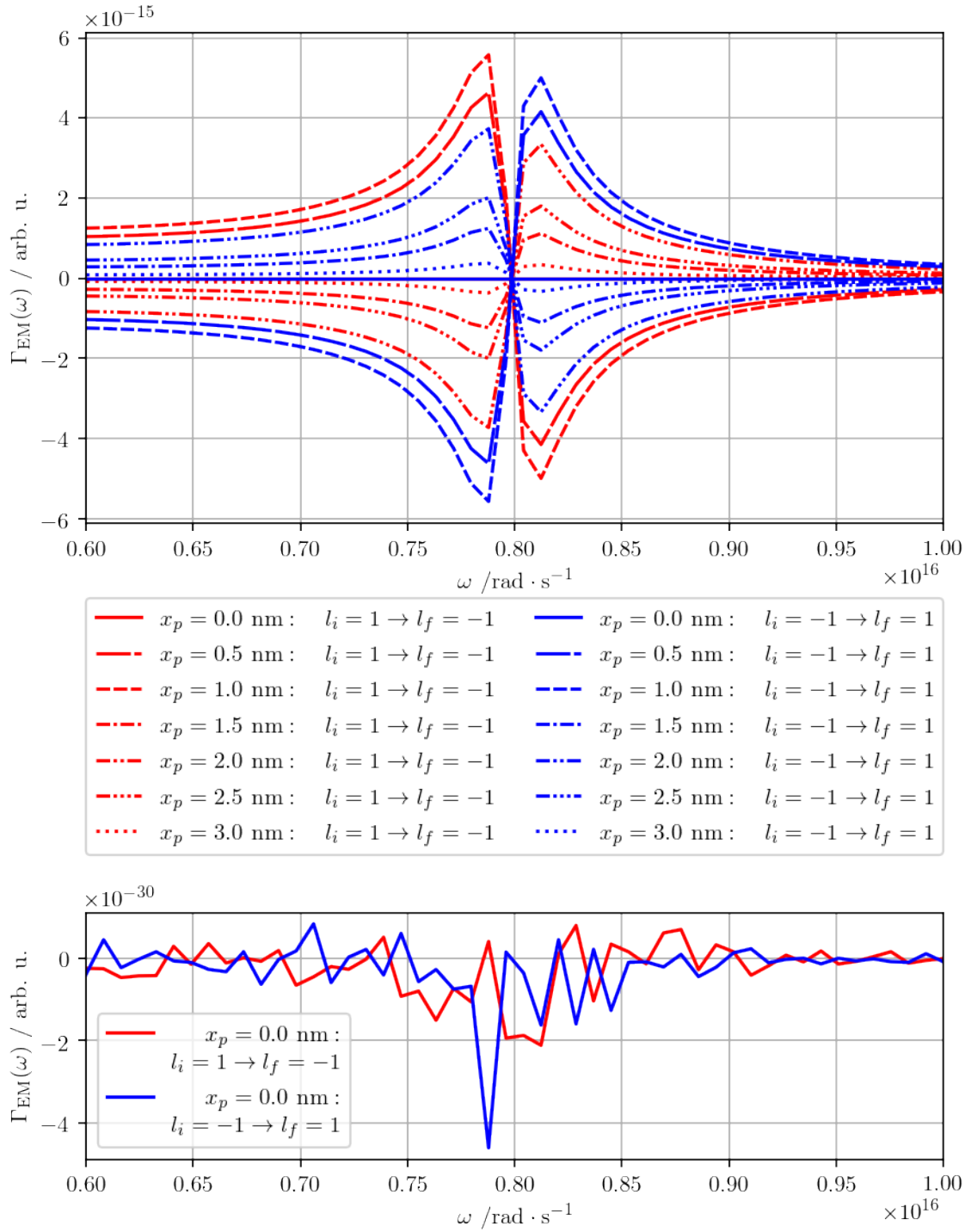


Figure 2.8: Dichroic spectra for the transfer of topological charge between +1 and -1 in both directions for different specimen positions. This figure has the highest information density. The first phenomenon we can observe is the opposition of dichroic intensities for opposite topological charge transitions (compare red curves with blue). Secondly, we can see (as is zoomed in the lower subplot) that when the specimen is in the center of the vortex, there is no response (and the computed numbers are only numerical noise). Finally, we can notice that the dependence of dichroic intensity on the position of the specimen is non-trivial, it even flips over zero (note that in one quadrant there are both red a blue lines). This means that in EELS spectrum, the specimen "looks" as "right-hand" for some distances and "left-hand" for others. See Figs. 2.9 and 2.10 for further detail.

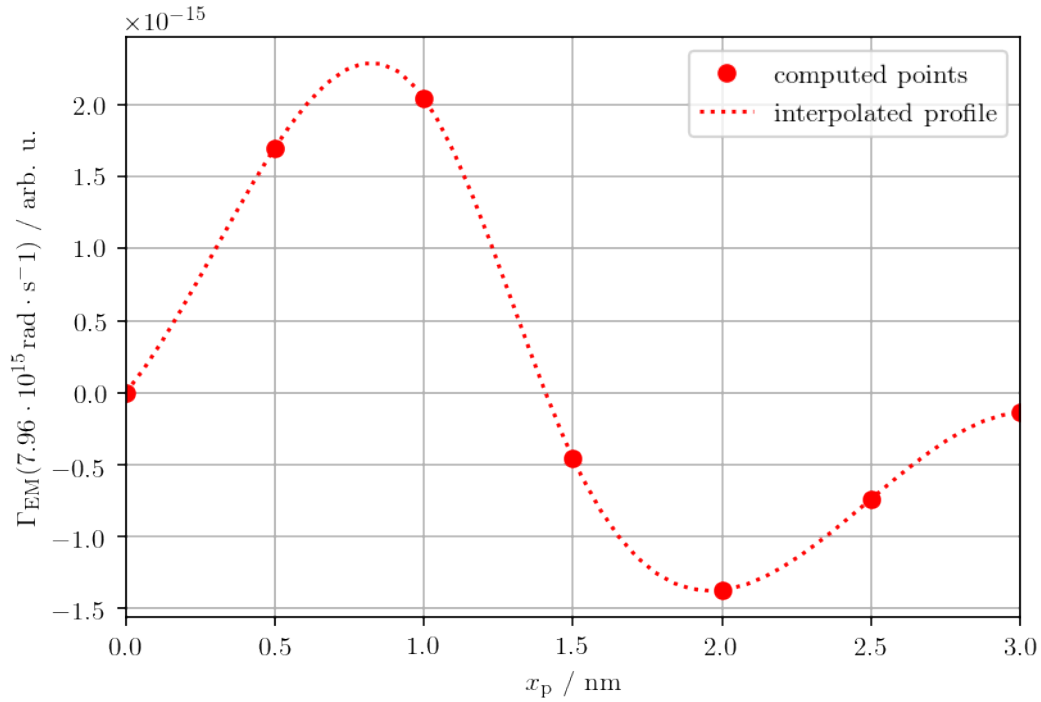


Figure 2.9: The dependence of dichroic response intensity on the position of specimen x_p . To interpolate the profile a quadratic spline was used, which means the interpolated profile should be viewed critically. In general, however, the overall trend should be respected.

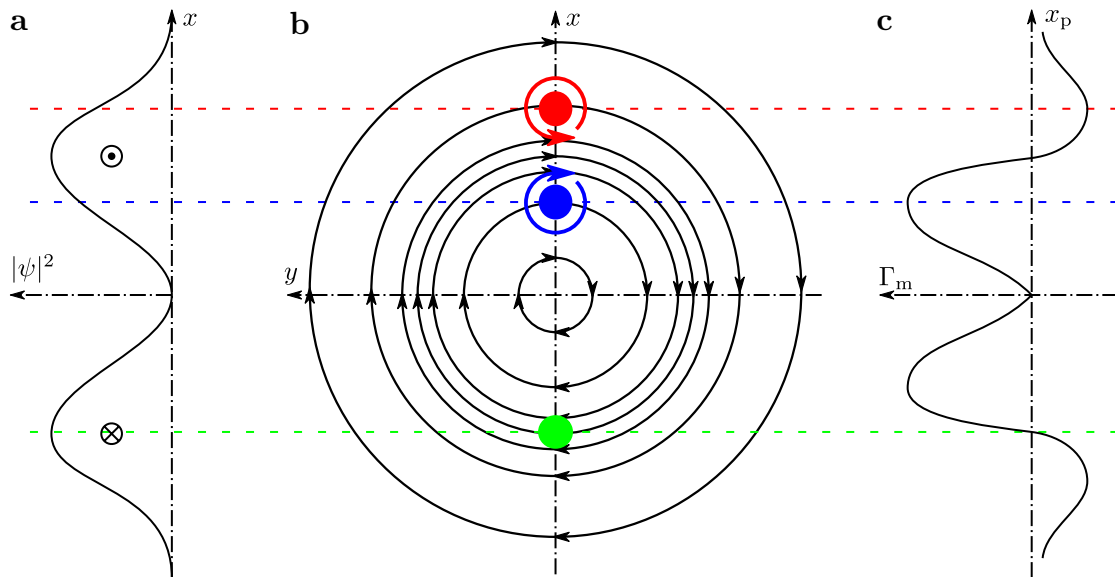


Figure 2.10: Intuition for the dependence of response intensity on the position of the specimen. a) Probability density of vortex. b) Scheme of vortex circulating around its center. Specimens (in colour "feel" the vorticity of the vortex differently depending on their position relative to the main maximum of probability density and can be "spun" in both clockwise and anticlockwise directions. c) Relative intensity of dichroic response dependent on the position of the specimen.

Chapter 3

Numerical Model

In this chapter, we present a model for EELS of VEB interacting with a 3D chiral metallic nanostructure. The proposed experiment is very similar to the previous one stated in Ch. 2. The only yet major difference is that the specimen is not a point-like polarizable particle which can be moved in the beam's profile, but a chirally arranged assembly of two metallic nanorods, see Fig. 3.1 for exact configuration and dimensions. Due to the complexity of the problem gained by the introduction of a specific geometry, we have to abandon (semi)analytical methods and approach the problem numerically.

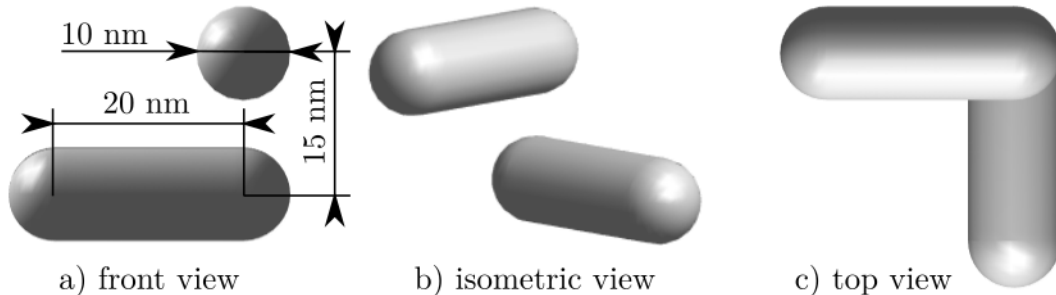


Figure 3.1: Probed chiral nanostructure consisting of two silver rods perpendicular to each other and vertically shifted in respect to each other. Note that the mirror image of this structure is incongruent to the original. In our implementation of calculation, the electron impinges on this structure from the bottom.

As we discussed previously, electron impinging on a metallic nanostructure is able to excite plasmonic modes. Plasmons are quasiparticles emerging from solving the Hamiltonian of the electron gas in metal and can be understood as collective excitations of charge in the material. They are of two flavours. The first flavour is bulk plasmons which we neglect in our calculations [29]. The second type of plasmons is surface plasmons. These form on a metal-dielectric interface and the oscillations of the charge are bound to the surface of the metal. Further, we refer to surface plasmons only as plasmons. When the material is constrained in all three dimensions, particle plasmons emerge. The excitation then takes the form of a standing wave (i.e. is decomposed in stationary modes). Properties of such oscillations depend heavily on the geometry of the particle in which plasmons are created. If multiple particles are present, plasmons on their surfaces often couple together. Plasmons are associated with an evanescent field of high intensity near the surface of the particle (especially around sharp edges). This field can be used to strengthen response in optical

systems (e.g. in photovoltaics or in a scanning near field optical microscope (SNOM)) by concentrating the field in volume [11].

As was briefly explained, plasmons are important material excitations applicable in a wide variety of technologies essential for everyday life in 21st century. They are often studied in STEM (TEM), particularly with EELS. The usage of VEBs instead of standard beams with zero OAM, which we model, opens a new degree of freedom in plasmon analysis. That will, hopefully, lead to a deeper understanding of the electromagnetic response of plasmonic structures, particularly chiral ones, which are expected to yield dichroic signals when probed by electron beams carrying non-zero OAM.

3.1 Boundary Element Method

In this section, we mostly take over the concepts from [11]. To model plasmons, one has to find plasmonic modes by solving Maxwell's equations. One of the methods which can be used to solve differential equations numerically is Boundary Element Method (BEM). Simply stated, in BEM all interfaces (boundaries) are discretised and Maxwell's equations are numerically solved for stated boundary conditions on each finite face of the boundary. In the boundary conditions, not only the geometry of the problem but also the dielectric constants of media across the interfaces are contained.

In our case, we consider small nanostructures, for which we use the quasistatic approximation leading to solving Laplace's equation

$$\nabla^2 \Phi = 0 \quad (3.1)$$

for the scalar potential Φ by assuming zero space charge in all environments. The solution to this equation can be written in the general form of

$$\Phi(\mathbf{r}) = \Phi_{\text{ext}}(\mathbf{r}) + \oint_{\partial V} d^2\mathbf{s} G(\mathbf{r}, \mathbf{s}) \sigma(\mathbf{s}) \quad (3.2)$$

for any point in space \mathbf{r} , where to the external potential $\Phi_{\text{ext}}(\mathbf{r})$ we add the contribution from the charge distribution on the surface of particle ∂V by integrating the Green's function G multiplied by the charge density σ over all the surface elements $d^2\mathbf{s}$ of the boundary.

From boundary continuity conditions for fields (i.e. from Maxwell's equations) and charge density one can derive a boundary integral equation of the form

$$\Lambda \sigma(\mathbf{s}) + \oint_{\partial V} d^2\mathbf{s}' \partial_{\mathbf{n}} [G(\mathbf{s}, \mathbf{s}')] \sigma(\mathbf{s}') = -\partial_{\mathbf{n}} \Phi_{\text{ext}}(\mathbf{s}), \quad (3.3)$$

where $\partial_{\mathbf{n}}$ denotes the derivative along the outer surface normal direction and for dielectric constants of inner and outer environment, ε_1 and ε_2 , respectively, $\Lambda = 2\pi(\varepsilon_2 + \varepsilon_1)/(\varepsilon_2 - \varepsilon_1)$. From here, we can already see that after the discretization (integrals taking the form of sums) we get (using ESR)

$$[\Lambda \delta_{ij} + (\partial_{\mathbf{n}} G)_{ij}] \sigma_j = -\partial_{\mathbf{n}} (\Phi_{\text{ext}})_i. \quad (3.4)$$

This is formally a problem of eigenvectors and eigenvalues for charge density. Practically it is a system of (generally dense) linear equations which can be solved through simple matrix inversion. Computers can do that very well and fast nowadays.

There exist many BEM solvers. One of them, widely used and especially well-equipped for dealing with plasmonic problems including EELS is a toolbox for MATLAB called MNPBEM (for Metal Nano-Particle Boundary Element Method) [11, 12] which we used for our computations.

After defining the geometry and material characteristics of the studied system, we can call function `bemstateig` which returns several objects including eigenvectors (of pseudo-charge-density distributions corresponding to each little discretization face of the particle system) and eigenvalues (pseudoenergies which correspond to $2\pi\lambda$ for vacuum wavelength λ). Surface pseudocharge density is a density of charge located on the surface of the particle which is not necessarily the same but produces the same field as the real charge distribution.

3.2 Interaction of Electron Beam with the Specimen

From now on, we roughly follow [29]. As the electron passes in the vicinity of the specimen, it interacts with every charge in the space around it. When the plasmonic mode is excited in the particle, the charge is distributed inhomogeneously on the surface of the particle and a field (in the quasistatic approximation scalar potential) is generated. The Hamiltonian of the electron-field interaction can be written as an integral over the interaction volume (or in our case the surface of the particle) with charge density ρ

$$\hat{\mathbf{H}} = - \oint d^3\mathbf{r}' e \frac{\rho(\mathbf{r}')}{|\mathbf{r} - \mathbf{r}'|}. \quad (3.5)$$

Assuming a weak interaction, one can find, using Fermi's golden rule, the EELSF for the transition between well-defined initial ψ_i and range of final ψ_f states of the electron beam by summing over the assumed final states of electron (f) and all plasmonic modes (n) of the specimen.

$$\Gamma(E) \propto \sum_{f,n} \left| \iint d^3\mathbf{r} d^3\mathbf{r}' \frac{\psi_f^*(\mathbf{r}) \psi_i(\mathbf{r}')}{|\mathbf{r} - \mathbf{r}'|} \langle n | \rho(\mathbf{r}') | 0 \rangle \right|^2 \delta(E_f - E_i - E), \quad (3.6)$$

where $|n\rangle$ and $|0\rangle$ are the n^{th} and ground plasmonic states of the particle, respectively, E_f and E_0 are the eigenenergies of the n^{th} and ground plasmonic states, respectively and E is the transferred energy.

It is further possible to rewrite this term as

$$\Gamma(E) \propto \sum_f \iint d^3\mathbf{r} d^3\mathbf{r}' \psi_f(\mathbf{r}) \psi_i^*(\mathbf{r}') \text{Im} [-W(\mathbf{r}, \mathbf{r}', E)] \psi_f^*(\mathbf{r}') \psi_i(\mathbf{r}) \delta(E_f - E_i - E), \quad (3.7)$$

where

$$W(\mathbf{r}, \mathbf{r}', E) = \sum_n g_n(E) \Phi_n(\mathbf{r}) \Phi_n^*(\mathbf{r}') \quad (3.8)$$

is the screened interaction between an electron in \mathbf{r} and in \mathbf{r}' . It is calculated from the n^{th} plasmon eigenpotential Φ_n corresponding to the eigenvector of charge density. The factor

$$g_n(E) = \frac{-2}{\varepsilon(1 + \lambda_n) + (1 - \lambda_n)} \quad (3.9)$$

is called spectral function (i.e. the weight function) of n^{th} plasmonic mode. The presented form is valid assuming the unit relative permittivity of the environment surrounding the

particle of which relative permittivity is ε . In the expression we use the eigen-wavelengths λ_n of n^{th} plasmonic mode (these are the results from BEM solution). [6]

In the non-recoil approximation (meaning that the z -perpendicular wave vector is negligible in comparison to the projection of the wave vector to z axis, which is well fulfilled for fast electrons) the last expression for EELS (3.7) can be significantly simplified for a particular (vortex) electron state transition $\psi_i \rightarrow \psi_f$ to the form

$$\Gamma_{i \rightarrow f}(E) \propto \sum_n \text{Im} [-g_n(E)] \left| \iint dx dy \psi_f(x, y) \Phi_n(x, y, \omega) \psi_i^*(x, y) \right|^2, \quad (3.10)$$

where $\Phi_n(x, y, \omega)$ is the z -Fourier transform of the n^{th} plasmon eigenpotential which emerged from the integration along the z direction. It can be calculated by integrating over all the charge densities σ on all of boundary surfaces S as

$$\Phi_n(\mathbf{r}_\perp, \omega) = 2 \oint_S d^2\mathbf{s} \sigma_n(\mathbf{s}) e^{-i\omega s_z/v} K_0 \left(\frac{\omega |\mathbf{r}_\perp - \mathbf{s}_\perp|}{v} \right), \quad (3.11)$$

where the transferred energy $E = \hbar\omega$, v is the speed of electron and in the argument of modified Bessel function of the second kind of order 0, K_0 , we denote the z -perpendicular projections by symbol \perp [6].

In our calculations, we assume the same as in the previous section – that the initial and final states of the electron beam are VEBs of form (1.18). More precisely, we are even assuming the same wave functions before and after the interaction.

3.3 Implementation

To implement the model for EELSF of VEB interacting with the chiral nanostructure shown in Fig. 3.1 we first needed to find the eigenstates of plasmons in this particle. For this purpose, a toolbox MNPBEM for MATLAB was used [11, 12]. After the extraction of charge eigendensities (eigenvectors) and eigenenergies (eigenvalues) together with positions and areas of modelled particle's faces, we have moved to PYTHON.

Libraries NUMPY, SCIPY and MATPLOTLIB were used in the computation scripts. The first thing to do was to calculate the g -factors according to Eq. (3.9) for the range of possible frequencies ω . In Fig. 3.2 we have plotted g -factors over the frequency domain for the first 15 plasmonic modes. We can easily see in the graph that if we restrict our studied interval of frequencies to $3 \cdot 10^{15} \text{ rad} \cdot \text{s}^{-1} - 5.5 \cdot 10^{15} \text{ rad} \cdot \text{s}^{-1}$, we can study only the effect of the first two plasmonic modes since the influence of higher modes is negligible. The two g -factors over the constrained interval of frequencies are plotted in Fig. 3.3.

After the g -factors were calculated, the z -Fourier transforms of first two chosen potentials $\Phi_n(\omega)$ produced by the n^{th} plasmonic mode driven on frequency ω were calculated from Eq. (3.11). Looking at the profiles of potentials in Fig. 3.4 and considering the fact that their resonant frequencies (eigenenergies) are close (see Figs. 3.2 and 3.3) we can interpret them as the bonding ($n = 1$) and anti-bonding ($n = 2$) modes of the two nanorods.

The next step was the calculation of the initial and final VEB wave function from Eq. (1.18) assuming final aperture widths for the preparation phase plate and for the collector so that the divergence of the beam is 3 mrad for energy 60 keV corresponding to speed $0.446c$. The wave function of the considered VEB is plotted in Fig. 3.5 in the same spatial range as the potentials. Note that in the calculations presented in this thesis, only the main

3.3. IMPLEMENTATION

maximum of the wave function has a reasonable effect when calculating the EELSF since by assuming the same wave functions before and after the interaction, as we did, we are effectively taking a square of the module in (3.10).

Finally, EELSFs presented in the next section were calculated according to Eq. (3.10).

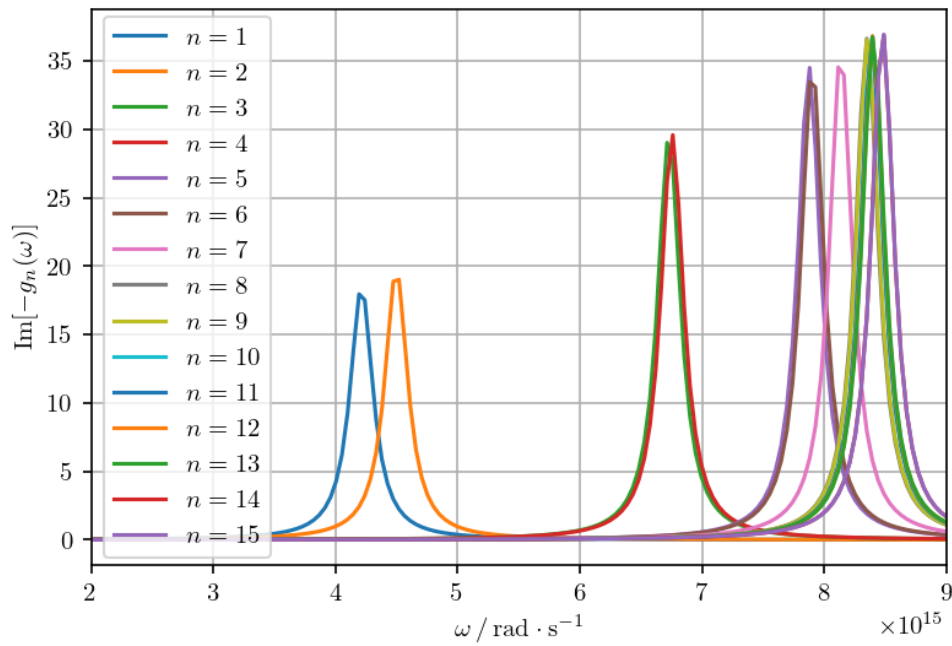


Figure 3.2: Spectral function g (its negative imaginary part) profiles over frequency ω domain for first 15 plasmonic modes n .

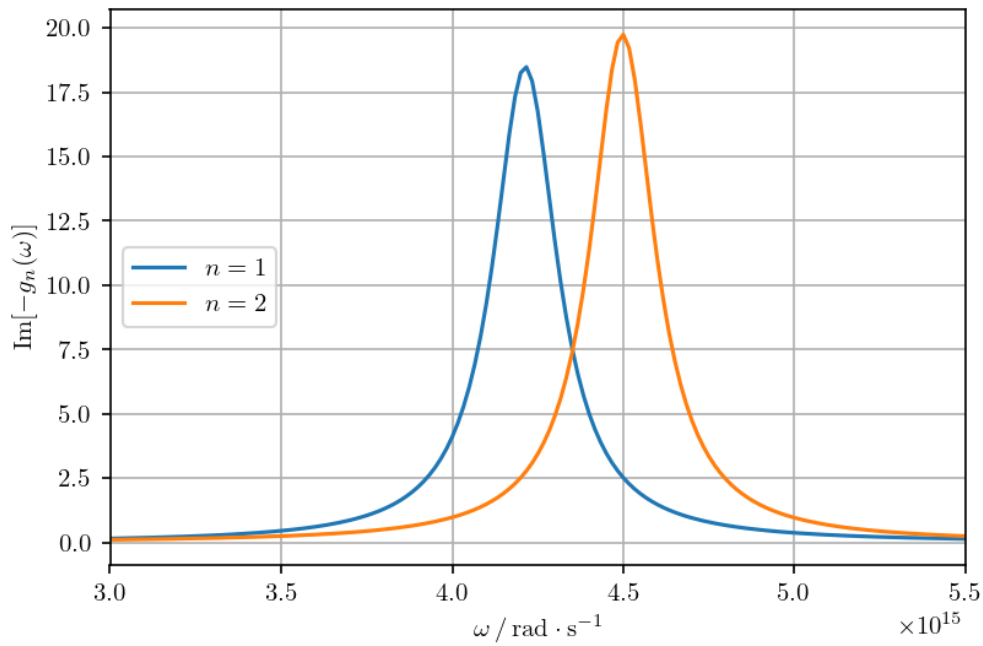


Figure 3.3: Spectral function g (its negative imaginary part) profiles over frequency ω interval constrained so that only the first two plasmonic modes n are significant.

3.3. IMPLEMENTATION

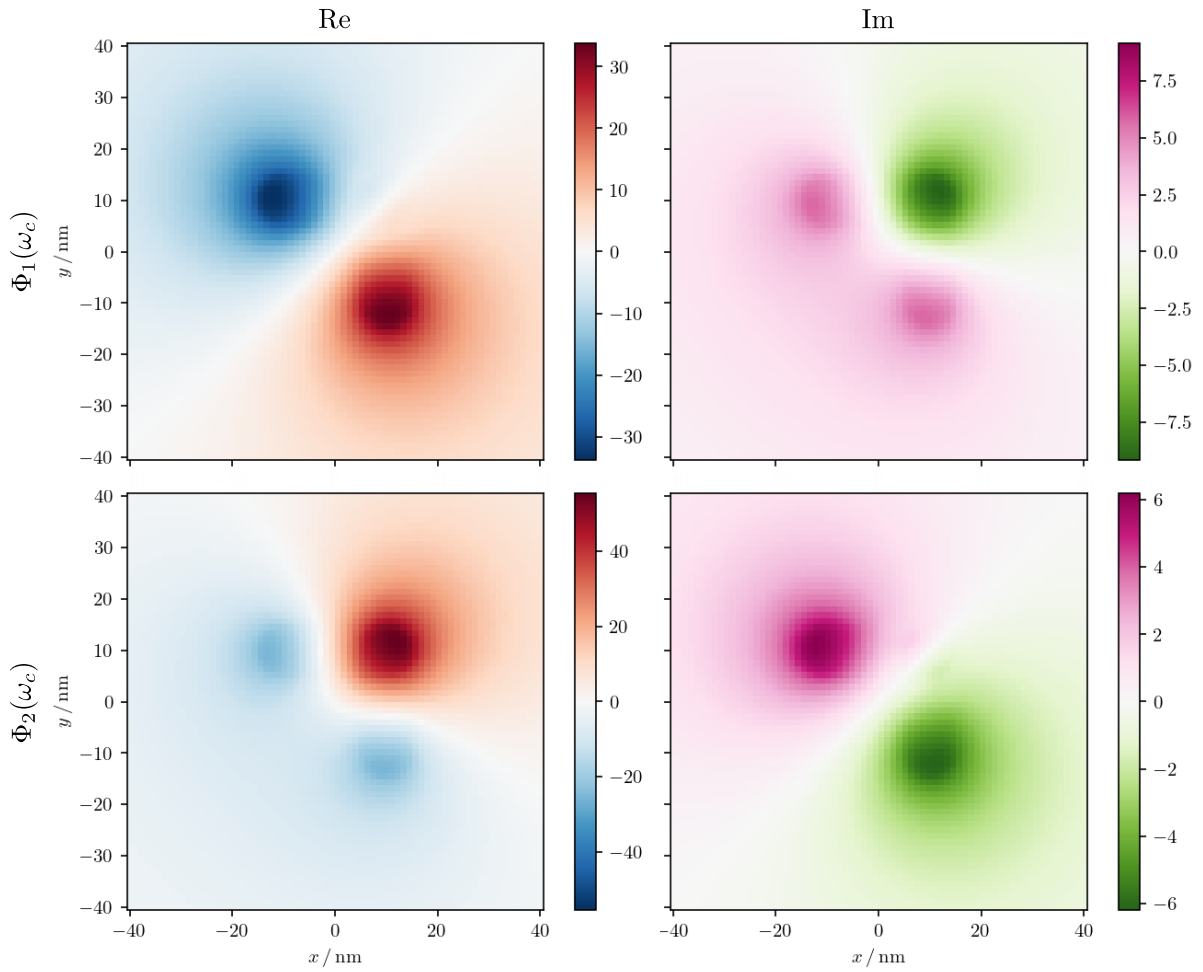


Figure 3.4: z -Fourier transform of potentials produced by the first two plasmonic modes driven by frequency $\omega_c = 4.5 \cdot 10^{15} \text{ rad} \cdot \text{s}^{-1}$. In the left columns, we can see real parts and in the right imaginary parts of potentials.

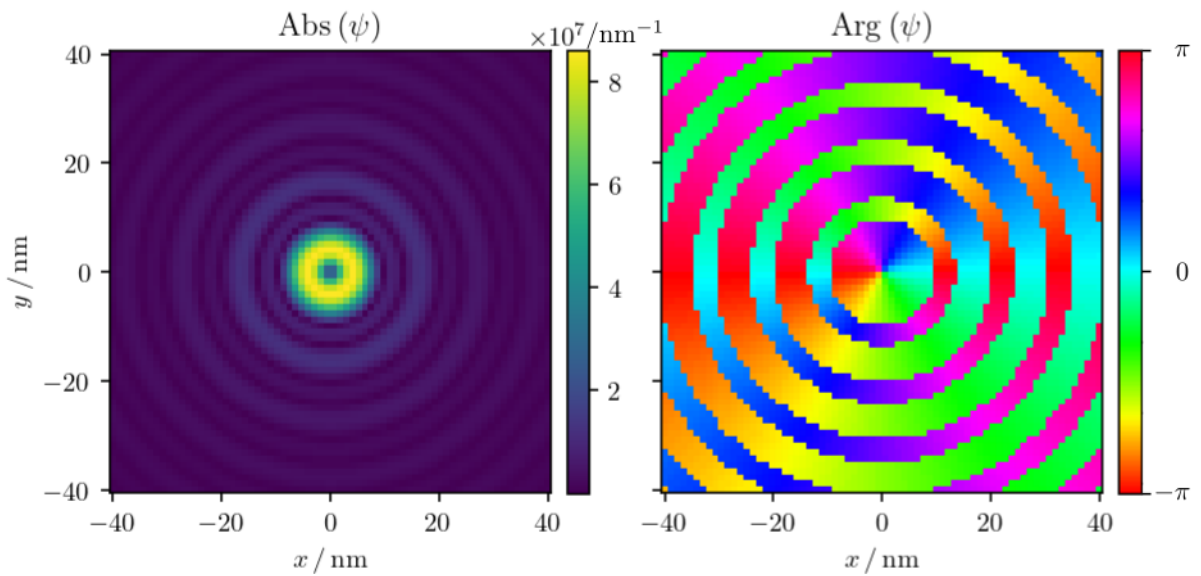


Figure 3.5: The wave function of the assumed VEB. Amplitude (left) and phase (right).

3.4 Results

In the last section of this thesis, we present computed EELS spectra of VEBs with non-changing topological charges ± 1 interacting with the chiral nanostructure consisting of two silver rods shown in Fig. 3.1. As well as in the previous chapter, we study the dependence of signal on the position of the center of the vortex relative to the specimen. In the beginning we shall stress that all spectra are theoretical spectra without consideration of bulk losses caused by the transition of the electron through the metal. We thus consider only the interaction of electron with the field produced by localized surface plasmons excited in the structure. This should be kept in mind especially when analyzing spectra gained for positions of vortex center near and in the particles.

Compared to Ch. 2 where we presented only certain contributions to the spectra coming from different polarizability terms, in this chapter full spectra are presented. We thus handle the term dichroism more precisely and define the (relative) dichroic spectrum between two spectra Γ_1 and Γ_2 as

$$D(\omega) = \frac{\Gamma_2(\omega) - \Gamma_1(\omega)}{\Gamma_2(\omega) + \Gamma_1(\omega)}. \quad (3.12)$$

In all presented spectra in this section we stick to the following conventions. All figures have two different y -axes. The left one (in purple) is an axis for EELSFs Γ which are plotted in red for VEBs with topological charge $l_i = l_f = +1$ (right-handed) and in blue for VEBs with $l_i = l_f = -1$ (left-handed). The right axes in black describe the gained dichroic spectrum D between left- and right-handed vortex, also plotted in solid black line. Note that this axis is naturally relative (meaning that the minimal and maximal possible values are -1 and 1, respectively). The position of the VEB's center is denoted x_c and y_c and is illustrated by the position of symbol $\textcircled{\odot}$ (denoting the position of the vortex center) relative to the studied nanostructure.

Now we will describe all presented spectra shown in Figs. 3.6–3.12. In the first spectrum shown in Fig. 3.6 (VEB position $x_c = y_c = -20$ nm) we can see that EELSF for both right-handed and left-handed VEBs are very similar, however, dichroism is weak. In both cases, major contribution to the spectrum comes from the first (bonding) plasmonic mode. Contribution of the second is noticeable as the little bump on the right side of the peak.

In Fig. 3.7 spectra for VEB position $x_c = y_c = -10$ nm (this is approximately in the middle of the structure's "cavity") are shown. Here, dichroism between left- and right-handed VEBs becomes very prominent. The extremity of the dichroic spectrum reaches up to -50% . This means that for the resonant frequency of the second mode, left-handed ($l = -1$) VEB has response three times as high as the right-handed ($l = +1$). This corresponds to our intuition, which says that the response will be higher if the current helix of VEB is oriented "the same way" as the "helix" of the specimen, see Fig 3.13.

When the VEB was centered in $x_c = y_c = 0$ nm (Fig. 3.8). The response moved to the second mode (and for the first there is only the little bump) for both handedness of vortex and the dichroism is very subtle.

As the VEB touches the "inner angle" of structure in $x_c = y_c = 10$ nm (Fig. 3.9) dichroism reappears. This time, the signal from the second (anti-bonding) mode is much higher for the right-handed ($l = +1$) vortex and the main peak of dichroic spectrum corresponds to the second plasmonic mode resonant frequency.

Moving to the other side of the structure, spectra in Figs. 3.10, 3.11 and 3.12 for $x_c = y_c = 20$ nm, 25 nm and 30 nm, respectively, are very similar. The main difference is in the

3.4. RESULTS

total magnitude of EELSFs. the dichroic signal, however is almost the same for all three positions of vortex center. Dichroism is most prominent for the first plasmonic mode since the left-handed ($l = -1$) vortex has much higher response intensity and in its spectrum two prominent peaks emerge, compared to the right-handed ($l = +1$) vortex spectrum where only small bump is present in place of the first mode.

The main conclusion we can make here is that (similarly as in previous section) the dependence of the dichroic response on the relative position of VEB center and the probed structure is non-trivial and we can get opposite dichroic spectra for different position of VEB's center relative to the specimen. Compare Figs. 3.7 for $x_c = y_c = -10$ nm vs. 3.10 for $x_c = y_c = 20$ nm.

An intuitive understanding of the discussed interactions and the emergence of dichroism can be gained in Fig. 3.13.

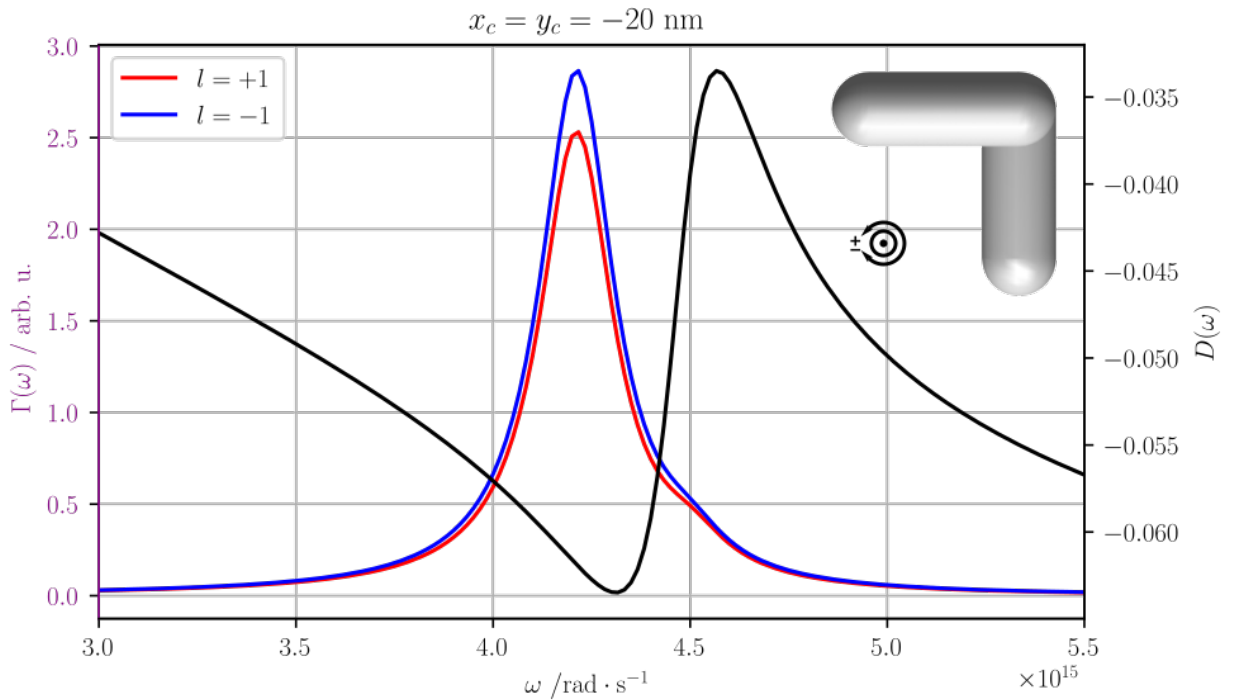


Figure 3.6: EELS (red and blue) and dichroic (black) spectra for interaction of VEBs (with topological charges +1 and -1 (red and blue respectively) positioned in $x_c = y_c = -20$ nm with chiral nanostructure.

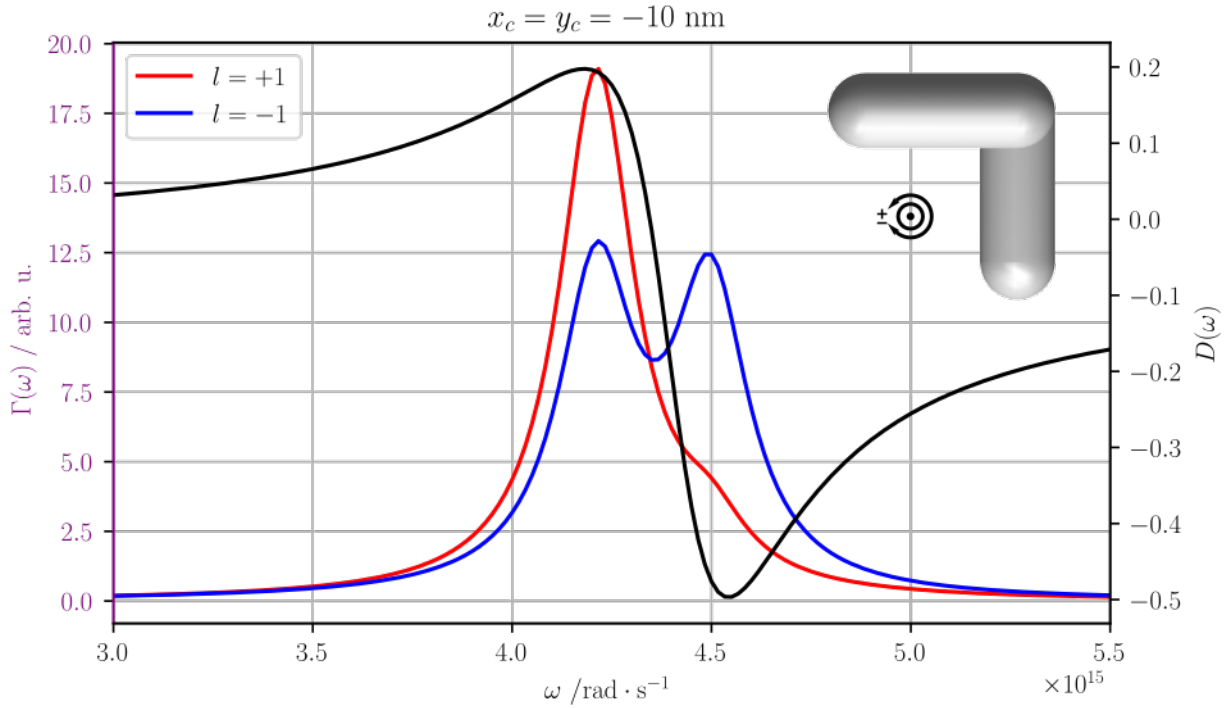


Figure 3.7: EELS (red and blue) and dichroic (black) spectra for interaction of VEBs (with topological charges $+1$ and -1 (red and blue respectively) positioned in $x_c = y_c = -10 \text{ nm}$ with chiral nanostructure.

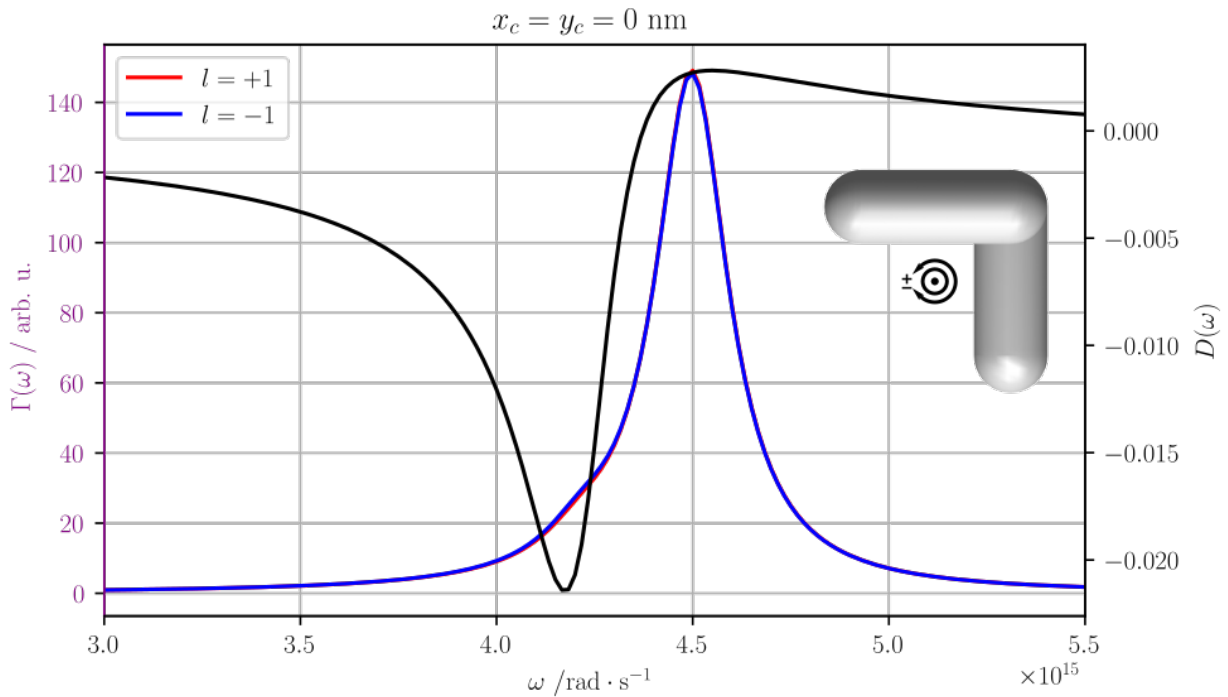


Figure 3.8: EELS (red and blue) and dichroic (black) spectra for interaction of VEBs (with topological charges $+1$ and -1 (red and blue respectively) positioned in $x_c = y_c = 0 \text{ nm}$ with chiral nanostructure.

3.4. RESULTS

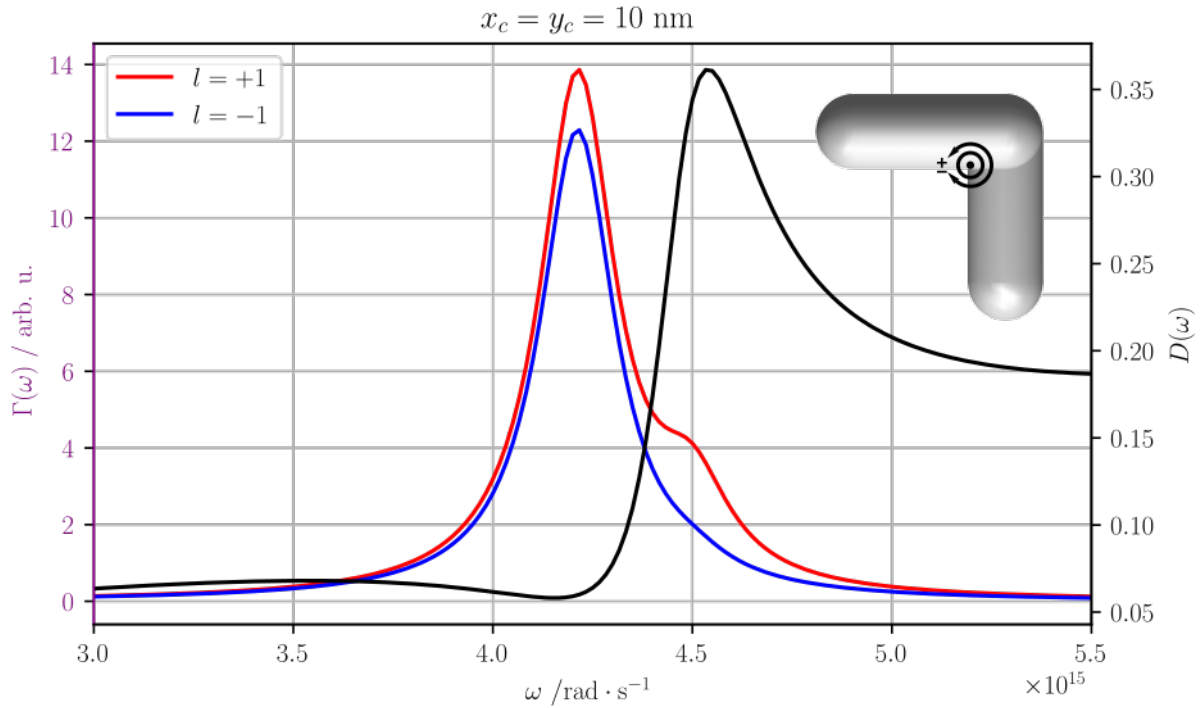


Figure 3.9: EELS (red and blue) and dichroic (black) spectra for interaction of VEBs (with topological charges +1 and -1 (red and blue respectively) positioned in $x_c = y_c = 10 \text{ nm}$ with chiral nanostructure.

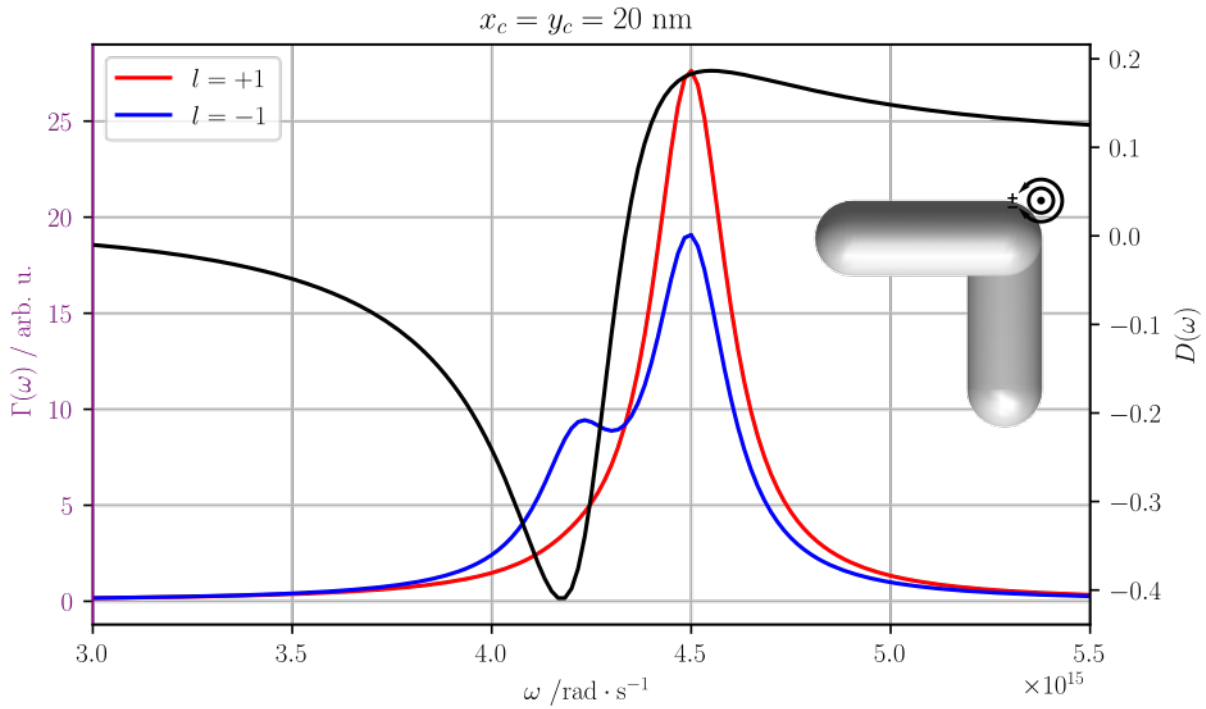


Figure 3.10: EELS (red and blue) and dichroic (black) spectra for interaction of VEBs (with topological charges +1 and -1 (red and blue respectively) positioned in $x_c = y_c = 20 \text{ nm}$ with chiral nanostructure.

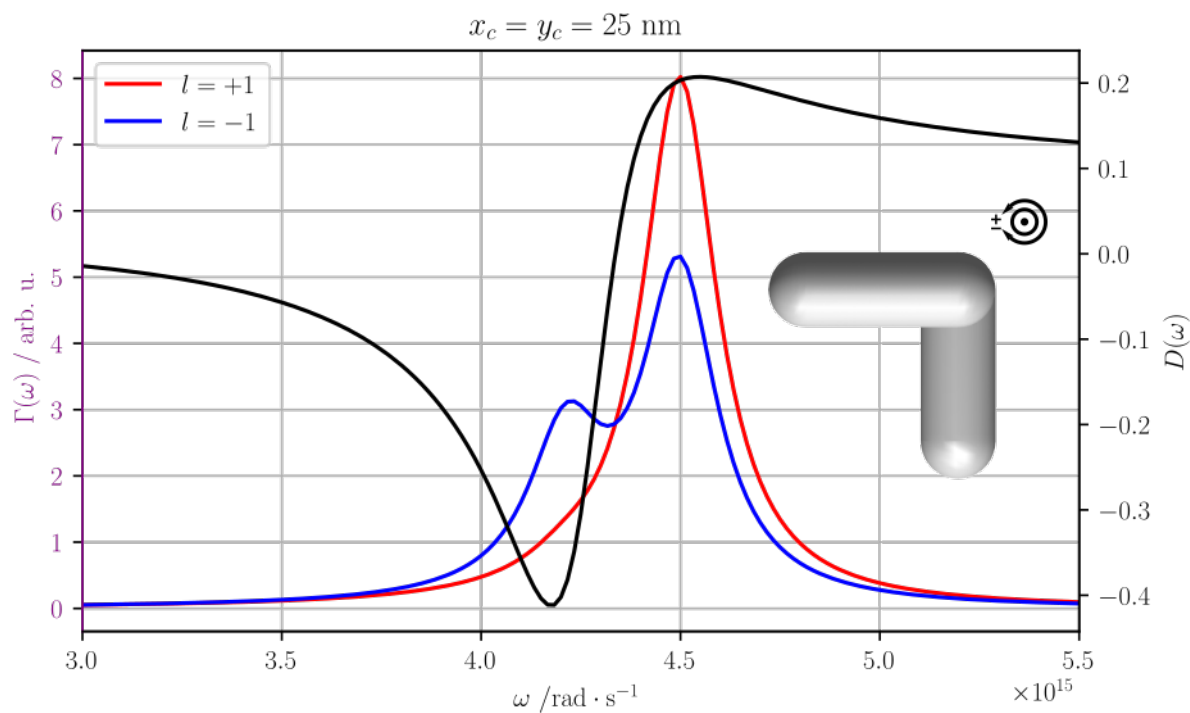


Figure 3.11: EELS (red and blue) and dichroic (black) spectra for interaction of VEBs (with topological charges $+1$ and -1 (red and blue respectively) positioned in $x_c = y_c = 25 \text{ nm}$ with chiral nanostructure.

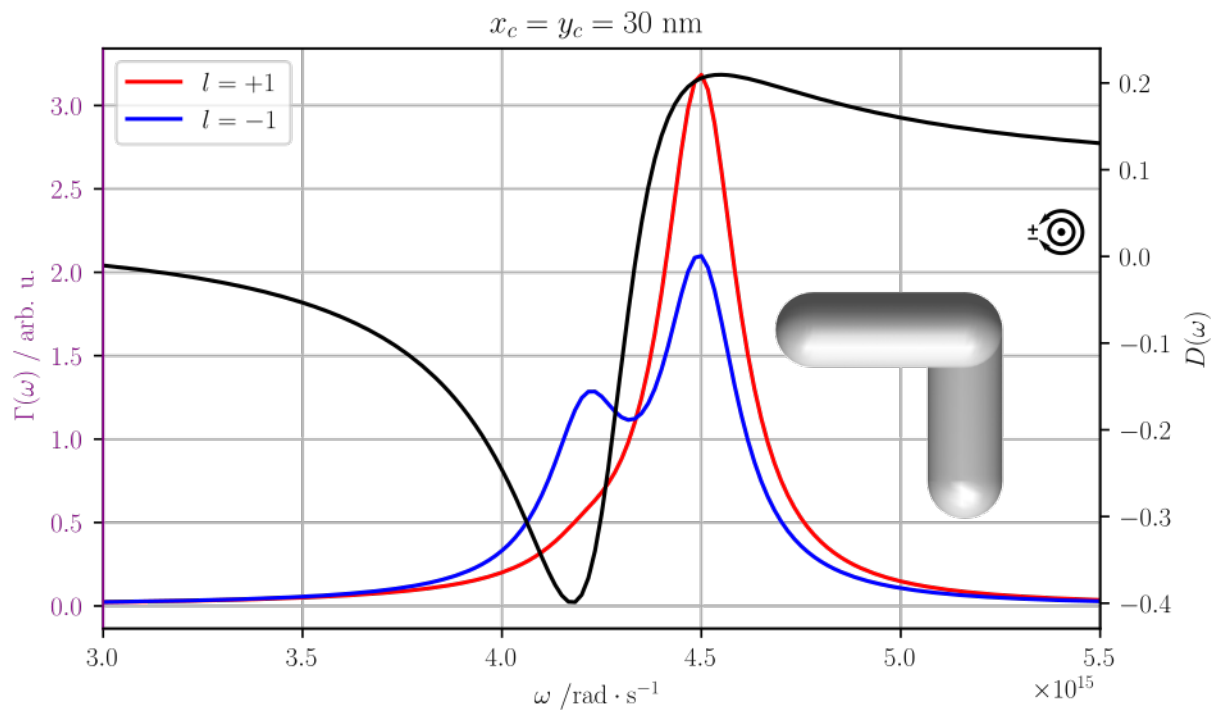


Figure 3.12: EELS (red and blue) and dichroic (black) spectra for interaction of VEBs (with topological charges $+1$ and -1 (red and blue respectively) positioned in $x_c = y_c = 30 \text{ nm}$ with chiral nanostructure.

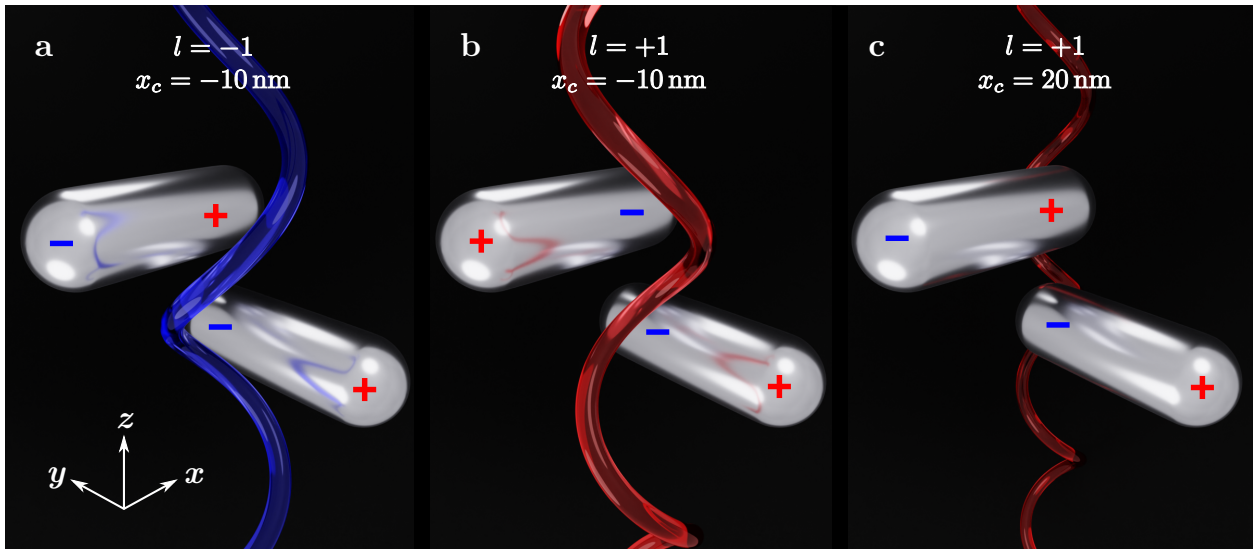


Figure 3.13: VEBs interacting with finite-size chiral specimens. Purpose of this figure is to gain an intuitive understanding of what is happening when VEBs interact with finite-size chiral specimen and why the dichroism emerges. Note that for illustrative purposes, the pitch of the helix (VEB) is not to scale. In reality, the pitch is so high that in this scale it would be unrecognizable. In subfigure (a) corresponding to the spectrum in Fig. 3.7, a left-handed beam centered in the middle of the structure creates a field acting on the charges in the rods. Intuitively, it can be seen that if a dipole forms on the bottom rod, the dipole on the upper rod will form so that opposite charges are near the gap (see the ascension direction of the helix and the “step” formed by the rods). This is the anti-symmetric (or anti-bonding) plasmon mode (with higher energy). An opposite situation occurs when the right-handed vortex impinges on the specimen (b). The dipoles formed on the rods now correspond to the symmetric (bonding) mode with the same charges near the gap. However, when we move the vortex center on the other side of the specimen (c) corresponding to the spectrum shown in Fig. 3.10, the (anti-)symmetry between the ascension of the VEB and the specimen is reversed. This leads to preferential excitation of the anti-bonding mode again.

Summary

In this thesis we studied the interaction of vortex electron beams (VEBs) carrying orbital angular momentum (OAM) with chiral specimens.

In the first and second chapter of our work, we modelled the electron energy loss spectrum (EELS) for the interaction of an extended vortex electron beam with a point-like chiral specimen. We proposed to use an OAM filter after the interaction to choose one particular vortex state from the superposition of all possible states in which the electron exists after the interaction. We studied the influence of initial OAM and its change together with position of the specimen relative to the vortex center on the spectra. When the specimen is chiral (i.e. its polarizability tensor enables the induction of magnetic dipole by electric field et vice versa) we observe significant dichroism. The most important finding is the non-trivial dependence of the dichroism intensity on the position of the specimen relative to the vortex center.

The third (and the last) chapter of this thesis describes a little different experiment. The setup is the same as for the point-like specimen, however the specimen is changed to a nanostructure of a finite size, which is "macroscopic" relative to the profile of the beam. We considered a simple specimen consisting of two silver nanorods perpendicular to each other in a step-like manner. We then probed this structure by left-handed and right-handed unfocused VEBs centered in different points. We found that a strong dichroic signal emerges for some configurations. Depending on the position of the VEB's center, we can see the dichroism for both of studied plasmonic modes. It is thus essential to know exactly the configuration of the experiment to make any conclusions about the specimen and its chirality. These results are consistent with findings of Konečná in [14], where she modelled the interaction of perfectly focused VEB with a similar structure.

In the future we would like to compute more spectra using both point-like and finite size models by tweaking all possible parameters including but not limited to: a) relative positions of VEB and specimen both on the axis of "semi-symmetry" of the specimen and asymmetric positions; b) VEB parameters (e.g. the energy or focus width); c) initial OAM and the change of OAM of the VEB; d) collection parameters (width of collection parameters; possibility of not-employing the OAM filter); e) different spacing between the rods or totally different structures (e.g. metallic nanohelices). All in all, the overall robustness of the dichroic signal to tweaking of the parameters should be examined.

Appendix A

Mathematical Notes

A.1 Square Root Approximation

Assume an expression in a form of

$$\sqrt{1+x}, \tag{A.1}$$

where $x \ll 1$. By expanding it with Maclaurin series (Taylor series with the center in 0) we can write

$$\sqrt{1+x} = 1 + \frac{1}{2}x + O(x^2). \tag{A.2}$$

If x is sufficiently small, we can neglect $O(x^2)$ and write

$$\sqrt{1+x} \cong 1 + \frac{1}{2}x, \tag{A.3}$$

which is widely used in paraxial approximations.

A.2 Cylindrical Coordinates

It might be convenient to describe a problem in cylindrical coordinates rather than in Cartesian when there exists some kind of axial symmetry. Let z be the direction of the axis of symmetry. Then any vector \mathbf{r} described by Cartesian coordinates x , y and z can be described by new set of coordinates: radius r and angle of deviation from x axis denoted ϕ together with formerly used z (see Fig. A.1).

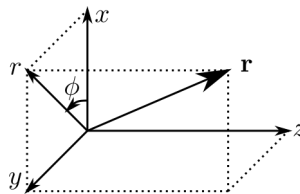


Figure A.1: Cylindrical coordinates.

The transformation equations are

$$\begin{aligned} x &= r \cos \phi, \\ y &= r \sin \phi, \quad \text{and} \\ z &= z. \end{aligned} \tag{A.4}$$

The inverse transformation rules are

$$\begin{aligned} r &= \sqrt{x^2 + y^2}, \\ \phi &= \arctan2(y, x), \quad \text{and} \\ z &= z. \end{aligned} \tag{A.5}$$

A.3 Evaluation of Integral (1.16) Using Jacobi–Anger Expansion

We will now focus on an integral of form

$$I = \int_0^{2\pi} d\phi e^{il\phi} e^{iQ \cos(\phi-\theta)}. \tag{A.6}$$

From [28] we get Jacobi-Anger expansion:

$$e^{iQ \cos(\phi)} = \sum_{n=-\infty}^{\infty} i^n J_n(Q) e^{in\phi}. \tag{A.7}$$

Substituting Eq. (A.7) into the Eq. (A.6) and after a rearrangement we get

$$I = \sum_{n=-\infty}^{\infty} i^n e^{-in\theta} J_n(Q) \int_0^{2\pi} d\phi e^{il\phi} e^{in\phi}. \tag{A.8}$$

From the residue theorem we can find (for $t \in (0, 2\pi)$) that

$$\int_0^{2\pi} d\phi e^{il\phi} e^{in\phi} = \oint_{z=e^{it}} dz z^{n+l-1} (-i) = \delta_{l,-n}. \tag{A.9}$$

This leads to the final result below. In the last step we used [7, Eq. 10.4.1].

$$I = 2\pi i^{-l} J_{-l}(Q) e^{il\theta} = 2\pi i^l J_l(Q) e^{il\theta}. \tag{A.10}$$

List of Abbreviations

1D, 2D, 3D, 4D,... one-, two- three- four-dimension(al)

BEM Boundary Element Method

CL Cathodoluminescence

EELS Electron Energy Loss Spectroscopy

EELSF Electron Energy Loss Spectral Function

EM Electromagnetic

LDOS local density of optical states

OAM Orbital Angular Momentum

PPP Programmable Phase Plate

SEM Scanning Electron Microscope

STEM Scanning Transmission Electron Microscopy

TEM Transmission Electron Microscopy

VE Vortex Electron, Electron Vortex, can be interchanged with VEB

VEB Vortex Electron Beam

References

- [1] G. ANZOLIN et al. “Method to measure off-axis displacements based on the analysis of the intensity distribution of a vortex beam.” In: *Physical Review A - Atomic, Molecular, and Optical Physics* 79 (3 2009). DOI: 10.1103/PhysRevA.79.033845.
- [2] A. ASENJO-GARCIA and F. J. G. D. ABAJO. “Dichroism in the interaction between vortex electron beams, plasmons, and molecules.” In: *Physical Review Letters* 113 (2014). DOI: 10.1103/PhysRevLett.113.066102.
- [3] R. A. BETH. “Direct Detection of the Angular Momentum of Light.” In: *Phys. Rev.* 48 (1935), pp. 471–471. DOI: 10.1103/PhysRev.48.471.
- [4] K. Y. BLOKH et al. *Theory and applications of free-electron vortex states*. 2017. DOI: 10.1016/j.physrep.2017.05.006.
- [5] M. BOSMAN et al. “Mapping surface plasmons at the nanometre scale with an electron beam.” In: *Nanotechnology* 18.16 (2007), p. 165505. DOI: 10.1088/0957-4484/18/16/165505.
- [6] G. BOUDARHAM and M. KO CIAK. “Modal decompositions of the local electromagnetic density of states and spatially resolved electron energy loss probability in terms of geometric modes.” In: *Phys. Rev. B* 85 (2012), p. 245447. DOI: 10.1103/PhysRevB.85.245447.
- [7] *NIST Digital Library of Mathematical Functions*. F. W. J. Olver, A. B. Olde Daalhuis, D. W. Lozier, B. I. Schneider, R. F. Boisvert, C. W. Clark, B. R. Miller, B. V. Saunders, H. S. Cohl, and M. A. McClain, eds. URL: <http://dlmf.nist.gov/>.
- [8] F. J. GARCÍA DE ABAJO. “Optical excitations in electron microscopy.” In: *Reviews of Modern Physics* 82 (2010), pp. 209–275. DOI: 10.1103/RevModPhys.82.209.
- [9] F. J. GARCÍA DE ABAJO and V. DI GIULIO. “Optical Excitations with Electron Beams: Challenges and Opportunities.” In: *ACS Photonics* 8 (2021), pp. 945–974. DOI: 10.1021/acsp Photonics.0c01950.
- [10] F. J. GARCÍA DE ABAJO and M. KO CIAK. “Probing the Photonic Local Density of States with Electron Energy Loss Spectroscopy.” In: *Phys. Rev. Lett.* 100 (2008), p. 106804. DOI: 10.1103/PhysRevLett.100.106804.
- [11] U. HOHENESTER and A. TRÜGLER. “MNPBEM – A Matlab toolbox for the simulation of plasmonic nanoparticles.” In: *Computer Physics Communications* 183 (2012), pp. 370–381. DOI: 10.1016/j.cpc.2011.09.009.
- [12] U. G. INSTITUT FÜR PHYSIK. *MNPBEM*. URL: <https://physik.uni-graz.at/de/mnpbem/> (visited on 05/15/2022).
- [13] J. KOMRSKA. *Difrakce*. 2007. URL: <http://physics.fme.vutbr.cz/~komrska/Difrakce/>.

-
- [14] A. KONEČNÁ. “Theoretical description of low-energy excitations in nanostructures as probed by fast electrons.” PhD thesis. University of the Basque Country, 2019.
- [15] A. KONEČNÁ et al. *Probing the electromagnetic response of dielectric antennas by vortex electron beams*. 2021.
- [16] Y. NOGUCHI et al. “Efficient Measurement of the Orbital-Angular-Momentum Spectrum of an Electron Beam via a Dammann Vortex Grating.” In: *Physical Review Applied* 12 (2019), p. 064062. DOI: 10.1103/PhysRevApplied.12.064062.
- [17] L. NOVOTNY and B. HECHT. *Principles of Nano-Optics*. 2nd ed. Cambridge University Press, 2012.
- [18] A. POLMAN et al. “Electron-beam spectroscopy for nanophotonics.” In: *Nature Materials* 18 (11 2019), pp. 1158–1171. DOI: 10.1038/s41563-019-0409-1.
- [19] K. SAITOH et al. “Production of electron vortex beams carrying large orbital angular momentum using spiral zone plates.” In: *Journal of Electron Microscopy* 61.3 (2012), pp. 171–177. DOI: 10.1093/jmicro/dfs036.
- [20] A. H. TAVABI et al. *Generation of electron vortex beams with over 1000 orbital angular momentum quanta using a tuneable electrostatic spiral phase plate*. 2022. DOI: 10.48550/ARXIV.2203.00477.
- [21] A. H. TAVABI et al. “Experimental Demonstration of an Electrostatic Orbital Angular Momentum Sorter for Electron Beams.” In: *Phys. Rev. Lett.* 126 (2021). DOI: 10.1103/PhysRevLett.126.094802.
- [22] M. UCHIDA and A. TONOMURA. “Generation of electron beams carrying orbital angular momentum.” In: *Nature* 464 (2010), pp. 737–739. DOI: 10.1038/nature08904.
- [23] G. M. VANACORE et al. “Ultrafast generation and control of an electron vortex beam via chiral plasmonic near fields.” In: *Nature Materials* 18 (2019), pp. 573–579. DOI: 10.1038/s41563-019-0336-1.
- [24] J. VERBEECK et al. “A new way of producing electron vortex probes for STEM.” In: *Ultramicroscopy* 113 (2012), pp. 83–87. DOI: 10.1016/j.ultramic.2011.10.008.
- [25] J. VERBEECK et al. “Production and application of electron vortex beams.” In: *Nature* 467 (2010), pp. 301–304. DOI: 10.1038/nature09366.
- [26] J. VERBEECK et al. “Demonstration of a 2×2 programmable phase plate for electrons.” In: *Ultramicroscopy* 190 (2018), pp. 58–65. DOI: <https://doi.org/10.1016/j.ultramic.2018.03.017>.
- [27] J. VERBEECK et al. “How to Manipulate Nanoparticles with an Electron Beam?” In: *Advanced Materials* 25 (2013), pp. 1114–1117. DOI: 10.1002/adma.201204206.
- [28] E. W. WEISSTEIN. *Jacobi-Anger Expansion*. *From MathWorld—A Wolfram Web Resource*. Last accessed 6 December 2021. 2021. URL: <https://mathworld.wolfram.com/Jacobi-AngerExpansion.html>.
- [29] M. ZANFROGNINI et al. “Orbital Angular Momentum and Energy Loss Characterization of Plasmonic Excitations in Metallic Nanostructures in TEM.” In: *ACS Photonics* 6 (2019), pp. 620–627. DOI: 10.1021/acsphotonics.9b00131.